Doctoral Thesis

Dosimetry of Internal Electric Field in Human Body for Exposure to Low- and Intermediate-Frequency Electromagnetic Fields

低周波-中間周波の環境電磁界による人体内誘導電界のドシメトリ評価

2024

Yoichi Sekiba

Contents

List of Figures

List of Tables

Chapter 1

Introduction

1.1. Background

The potential adverse health effects of exposure to electromagnetic fields have been of great concern. Around the 1980s, the WHO began to address the issue of the health effects of electromagnetic fields. Interest in the effects of artificial electromagnetic fields on the human body has largely focused on two frequency bands, the ELF (extremely low frequency) band and the RF (radio frequency) band, and many studies have been accumulated to elucidate these effects [1–6]. According to the WHO definition, ELF is below 300 kHz and RF is between 10 MHz and 300 GHz [7]. The interest in ELFs began in the late 1960s with concern over the health effects of commercial frequency electric fields around electric power facilities, and then shifted to commercial frequency magnetic fields in 1979 with epidemiological studies by American researchers [4]. Systematic research on RF has also been conducted in line with the rapid spread of wireless communications [3]. In the intermediate frequency band between 300 Hz and 10 MHz, which is between ELF and RF, there have been numerous studies on health effects with the spread of induction cooktops since the 1990s [8].

In particular, power transmission, distribution lines, and other electric power facilities are installed adjacent to the living areas of the general public. Thus, it is important to consider the protection of the human body from the electromagnetic fields generated from these facilities.

The frequencies of electromagnetic fields generated around major power transmission and distribution facilities are in the commercial frequency range (50 Hz or 60 Hz) and their harmonics. However, leaked electromagnetic fields in the intermediate frequency range exceeding several hundred kHz may occur around inverters for AC-to-DC conversion and wireless power transfer facilities. The dominant effect of electromagnetic fields from low frequencies to intermediate frequencies on the human body is nervous stimulation by induced currents at frequencies below 100 kHz.

Guidelines for the protection of the human body against electromagnetic fields are provided in international protection guidelines such as ICNIRP and IEEE standards, as described in the next section. In Japan, the regulation for the general public of magnetic fields around electric power facilities was introduced in 2011 in the ministerial ordinances related to electrical equipment in Japan [12] as described in section 1.1.2, referring to the regulation values of the ICNIRP guidelines. The safety of the general public living in the vicinity of electric power facilities and workers directly involved in electric power operations will be ensured through the elaboration of the regulation values in these international protection guidelines.

1.1.1. International Guidelines for Human Protection from Electromagnetic Fields

There are two international guidelines/standards that offer protection from environmental electromagnetic fields: the International Commission on Non-Ionizing Radiation Protection (ICNIRP) [9, 10] and the Institute of Electrical and Electronics Engineers (IEEE) standard C95.1^{TM}-2019 [11]. These guidelines are referenced in World Health Organization documents and establish limits for the induced in-situ electric fields within the human body for exposure to electromagnetic fields from 0 GHz to 300 GHz, including low-frequency and intermediate environmental (external) electronic and magnetic fields. In the low-frequency range, both external electric and magnetic fields induce an electric field in the human body governed by distinct physical laws [13]. When exposed to an electric field, surface charges induce a capacitive current; therefore, an electric field within the body [13]. Regarding magnetic field exposure, Faraday’s law indicates that eddy currents will occur within the body [13].

The limit for these induced electric fields is known as the "basic restriction" according to ICNIRP guidelines or “dosimetric references limit (DRL)” per the IEEE standard (hereinafter referred to as basic restriction). The basic restriction is derived from the threshold for nervous stimulation, factoring in a safety margin [14, 15]. The basic restrictions in the ICNIRP guidelines and IEEE standard are listed in Tables 1.1 and 1.2, respectively.

Table 1.1 Basic restrictions in ICNIRP guidelines up to 10 MHz.

Exposure characteristic	Body part	Frequency range	Induced electric field [V/m]
Occupational exposure	CNS of the head	1Hz – 10 Hz	$0.5/f$
		10 Hz – 25 Hz	0.05
		25 Hz – 400 Hz	$2\times10^{-3} f$
		400 Hz – 3 kHz	0.8
		3 kHz – 10 MHz	$2.7\times10^{-4} f$
	All tissue of head and whole body	1 Hz – 3 kHz	0.8
		3 kHz – 10 MHz	$2.7\times10^{-4} f$
General public exposure	CNS of the head	1Hz – 10 Hz	$0.1/f$
		10 Hz – 25 Hz	0.01
		25Hz – 1000 Hz	$0.4\times10^{-3} f$
		1000 Hz – 3 kHz	0.4
		3 kHz – 10MHz	$1.35\times10^{-4} f$
	All tissue of head and whole body	1 Hz – 3 kHz	0.4
		3 kHz – 10 MHz	$1.35\times10^{-4} f$

* f: frequency [Hz]

Table 1.2 Basic restrictions in IEEE standard up to 5 MHz

Exposed tissue	f_e [Hz]	General public condition	Controlled environment condition
		E_O [V/m-rms]	
Brain	20	5.89×10^{-3}	1.77×10^{-2}
Heart	167	0.943	0.943
Limb	3350	2.10	2.10
Other tissues	3350	0.701	2.10

*1: Limits for the electric field in the body are $E_i = E_O$ for frequencies $f \leqq f_e$ and $E_i = E_O (f / f_e)$ for frequencies $f \geq f_e$.

*2: In addition to the limits in this table, magnetic fields below 10 Hz are limited to a peak value of 167 mT (general public) and 500 mT (controlled environment).

In addition, permissible external field strength is determined separately for electric and magnetic field exposure, referred to as the “reference level” in the ICNIRP guidelines or “exposure reference level (ERL)” according to the IEEE standard (hereinafter referred to as reference level). The reference level is defined as the external electric/magnetic field that corresponds to the basic restriction because it is difficult to access internal quantities to make practical assessments. The reference levels in ICNIRP guidelines and the IEEE standard are listed in Tables 1.3 and 1.4, respectively.

Fig.1.1 shows comparison of basic restriction for general public and occupational (controlled environment) condition between ICNIRP guideline and IEEE standard. Fig.1.2 shows comparison of reference level for magnetic field and electric field between ICNIRP guideline and IEEE standard. As shown in these figures, there are differences between the ICNIRP guidelines and the IEEE standard for basic restrictions and reference levels, respectively, due to differences in the biological basis for the basic restrictions and the method used to derive the reference levels.

Table 1.3 Reference levels in ICNIRP guidelines up to 10 MHz.

Exposure characteristic	Frequency range	Electric field strength [kV/m]	Magnetic flux density [T]
Occupational exposure	1 Hz – 8 Hz	20	$0.2 / f^2$
	8 Hz – 25 Hz	20	$2.5\times10^{-2} / f$
	25Hz – 300 Hz	$5\times10^2 / f$	1×10^{-3}
	300 Hz – 3 kHz	$5\times10^2 / f$	$0.3 / f$
	3 kHz – 10 MHz	1.7×10^{-1}	1×10^{-4}
General public exposure	1 Hz – 8 Hz	5	$0.04 / f^2$
	8 Hz – 25 Hz	5	$0.5\times10^{-2} / f$
	25Hz – 50 Hz	5	0.2×10^{-3}
	50 Hz – 400 Hz	$2.5\times10^2 / f$	0.2×10^{-3}
	400 Hz – 3 kHz	$2.5\times10^2 / f$	$0.08 / f$
	3 kHz – 10MHz	0.83×10^{-1}	0.27×10^{-4}

* *f*: frequency [Hz]

Table 1.4 Reference levels in IEEE standard up to 5 MHz

(a) Electric field

Exposure characteristic	Frequency range	Electric field strength E [V/m]
General public condition	0 Hz - 368 Hz	5000
	368 Hz – 3 kHz	$1.84 \times 10^6 / f$
	3 kHz – 100 kHz	614
Controlled environment condition	0 Hz - 272 Hz	20000
	272 Hz – 2.953 kHz	$5.44 \times 10^6 / f$
	2.953 kHz – 100 kHz	1842

(b) Magnetic field

Exposed tissue	Frequency range	General public condition	Controlled environment condition
		Magnetic flux density B [mT]	
Head and torso	below 0.153 Hz	118	353
	0.153 Hz – 20 Hz	$18.1 / f$	$54.3 / f$
	20 Hz – 759 Hz	0.904	2.71
	759 Hz – 3350 Hz	$687 / f$	$2060 / f$
	3350 – 5 MHz	0.205	0.615
Limbs	below 10.7 Hz	353	353
	10.7 Hz – 3350 Hz	$3790 / f$	$3790 / f$
	3350 Hz – 5 MHz	1.13	1.13

* f: frequency [Hz]

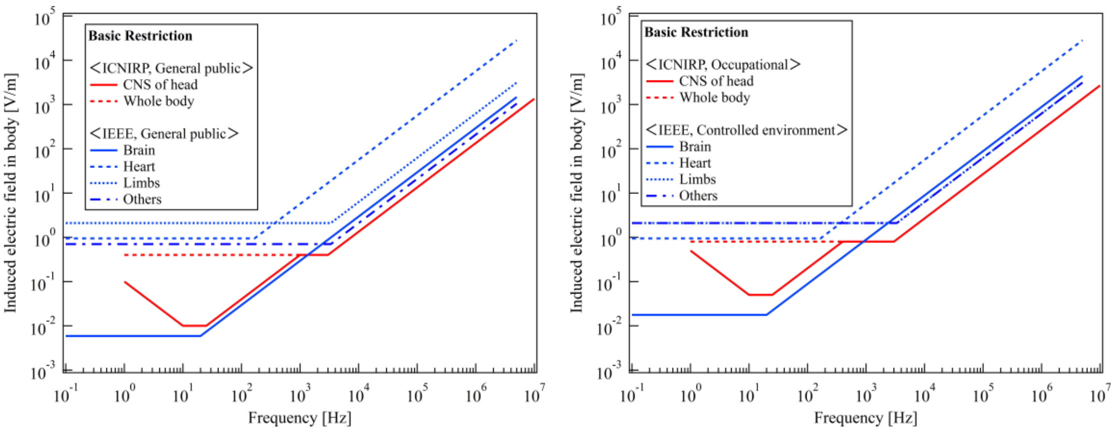

(a) (b)

Figure 1.1 Comparison of basic restriction for (a) general public and (b) occupational (controlled environment) condition between ICNIRP guideline and IEEE standard.

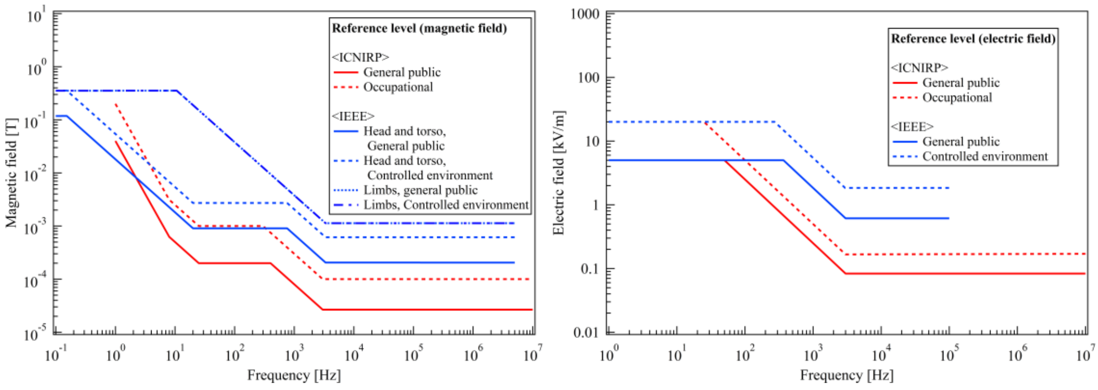

(a) (b)

Figure 1.2 Comparison of reference level for (a) magnetic field and (b) electric field between ICNIRP guideline and IEEE standard.

1.1.2. Ministerial Ordinances in Japan

The following limits for electric field strength and magnetic field strength of electrical equipment are specified in the Ministerial Ordinance establishing technical standards for electrical equipment based on the electricity business law in Japan [12]. The regulation for magnetic field strength was introduced in 2011 referring to the reference level for general public of the ICNIRP guidelines.

Regulations on Electric Field Strength

Extra high-voltage overhead lines shall be installed so that the electric field strength at one meter above the ground surface is less than 3 kV/m so that there is no danger of detection by humans due to electrostatic induction under normal conditions of use. (quoted from article 27 of the ministerial ordinance)

Regulations on Magnetic Field Strength

When transformers, switches, and similar devices or electric lines are installed in places other than power plants, power storage facilities, substations, switchyards, and places of demand, they shall be installed so that the average value of magnetic flux density in a space equivalent to the space occupied by a person in the vicinity of each of said electrical machinery and apparatus, etc. shall be 200 μT or less at commercial frequency so that there is no risk of affecting human health under normal conditions of use due to electromagnetic induction effects from these facility. (quoted from article 27-2 of the ministerial ordinance)

1.1.3. Related Previous Studies and Research Necessity

Differences between ICNIRP Guidelines and IEEE Standards

As described in Section 1.1.1, there are differences between the ICNIRP guidelines and the IEEE standard in terms of basic restrictions and reference levels, respectively. The reference levels of magnetic fields in the ICNIRP guidelines are the basis for magnetic field limits in domestic electric power facilities [12], and elaboration of international protection guidelines is important to ensure electromagnetic field safety for the public and electric power workers.

Issues Related to Reference Level Derivation

In the ICNIRP guidelines, the results of numerical computations performed using anatomical human models were used to derive reference levels of the basic restrictions [9]. However, the IEEE standard uses analytical solutions to determine the electric field produced by magnetic induction to relate basic restriction and reference levels. An elliptical cross-sectional model with homogeneous conductivity that simulates each part of the human body was employed [11]. Recently, a new IEEE working group (IEEE International Committee on Electromagnetic Safety Technical Committee 95 Subcommittee 6) has been formed to investigate the applicability of computations using anatomical human models in the derivation of reference levels. Accordingly, a previous study conducted an intercomparison of the electric fields induced in the anatomical human body by uniform magnetic fields of 50 Hz to 1 MHz among five different research groups [16]. In that study, the induced field strength exceeded the analytical solution by the homogeneous elliptic model defined in the IEEE standard at some body parts and frequencies. However, only magnetic fields alternating in the front-back direction of the human body were considered, and further confirmation of the IEEE reference level derivation process requires expansion of the conditions considered.

The elaboration of the reference level of the IEEE standard by applying the results of computation using the human body model will also contribute to correcting this discrepancy between the ICNIRP guidelines and the IEEE standard mentioned above.

Effect of Simultaneous Exposure to Electric and Magnetic Fields and their Phase Difference

The ICNIRP guidelines [9] note that induced electric fields by external electric and magnetic fields sum up vectorially. However, they also mention that such additive treatment is infrequently necessary, given the difference in the distributions of electrically and magnetically induced fields. As such, numerous dosimetric assessments have been reported based on single magnetic [17–31] or electric [32–41] field exposures. This assessment approach is justified as in most exposure scenarios, either electric or magnetic field coupling is dominant.

However, in practical scenarios such as under high-voltage overhead power lines (50 or 60 Hz), simultaneous exposure to electric and magnetic fields may occur. In such an environment, the induced electric fields in humans for respective exposure to electric and magnetic fields should be evaluated. The induced electric fields due to the electric field and magnetic field may either constructively or destructively interfere, depending on the location of the human body. These conditions have been evaluated using an anatomical human body model in previous studies [42, 43]. These studies suggested considering superposed electromagnetic fields for conservative evaluation because the induced electric field strength for simultaneous exposure may exceed that induced by a single component of electric and magnetic fields in some body parts. These studies assumed that the electric and magnetic fields are in phase. However, a phase difference exists between the current and the voltage induced by line impedance and power flow conditions [44, 45]. The impact of this phase difference between the electric and magnetic fields on the induced electric field in the body has not been quantitatively explored.

Necessity for Advancement of dosimetry methods for electric fields

Anatomical human body models with a resolution of 1–2 mm, which are generally used for conformity assessments of international standards, consist of millions to tens of millions of voxels, and a dosimetry is computationally expensive in terms of computer memory and time. Especially in the dosimetric analysis of low-frequency electric field exposure [32–41], the computational cost tends to be large due to the complexity of the physical process, in which surface charges generated on the human body surface by electrostatic induction induce capacitive currents in the body. Conventional dosimetric methods for exposure to electric fields include the quasi-static difference time domain (QS-FDTD) method [21], [34–36] and methods based on the scalar potential finite difference (SPFD) method [37, 38], both of which require the consideration of electrical quantities in the external space of the body in addition to the body, and thus require a huge computational cost. To efficiently solve the other research problems mentioned above, this computational burden must also be addressed as a practical issue.

In this regard, there are many examples of dosimetry for magnetic field [17–31], but few examples of dosimetry for electric field [32–41]. Establishment of a computationally efficient method for electric field dosimetry will make it possible to evaluate the overall effects of electromagnetic fields at low frequencies.

1.2. Contents of this Thesis

This study assessed the issues related to the validity of the reference levels of electromagnetic fields at low-to-intermediate frequencies in the international guidelines based on computational dosimetry applying anatomical human body models. The motivations of this study are as follows:

1. To develop improved computational methods for dosimetry of human exposure to electric fields with increased computational efficiency, thereby reducing computational time and memory. It enables a comprehensive evaluation of electromagnetic field effects at low frequencies.
2. To verify the consistency between the reference level and the basic restrictions in the IEEE standard by computational dosimetry using anatomical body models of adult males and females.
3. To evaluate the effect of simultaneous exposure to electric and magnetic fields and their phase difference on the induced electric field in the human body. It is especially important to assess whether the basic restriction of exposure guidelines is still met when considering the phase difference for simultaneous exposure.

By solving issue 1, the comprehensive dosimetry method for electric/magnetic fields at low frequencies can be strengthened, allowing for the study of issues 2 and 3. The discussion of 2 and 3 may provide important insights for the elaboration of the international protection guidelines.

The contents of this thesis are as follows.

Chapter 1 contains the background and motivation of this study.

Chapter 2 explains anatomical human models and computational methods. First, the anatomical three individual human models are presented. Next, the SPFD method, a computational method for deriving the induced electric field due to the magnetic field, and the post-processing method for the induced electric field are described. Finally, the acceleration of the computational process is presented.

Chapter 3 proposes a new dosimetry method for electric field exposure that combines the fast-multipole surface charge method and the SPFD method to reduce computational costs. The validity and performance of the proposed method are evaluated via comparisons with the conventional QS-FDTD method using an anatomical human body model.

Chapter 4 verifies the consistency between the reference level and the basic restrictions in the IEEE standard by dosimetry using anatomical human body models of adult males and females. A spatially uniform magnetic field with the strength of the reference level is applied to the human body model in the frequency range of 0.5 Hz to 5 MHz, and the induced electric fields in the body are evaluated via dosimetry analyses of the brain, heart, limbs, and other tissues of the body subject to the basic restrictions of the standard, and compared with the basic restrictions.

Chapter 5 examines the effects of phase differences of electromagnetic fields on induced electric fields in the body under conditions of simultaneous exposure to electromagnetic fields by dosimetry analyses using anatomical human body models of adult men, women, and children. Electric and magnetic fields with a frequency of 50 Hz and a phase difference of −90° to +90° are applied to a human body model with the strength equivalent to the reference level of ICNIRP guidelines and IEEE standards, and the induced electric field in the body is evaluated by dosimetry analyses and compared with the basic restrictions.

Chapter 6 summarizes this study.

Chapter 2

Models and Methods

2.1. Overview

In this thesis, we compute the induced electric fields by magnetic and electric field in the anatomical human models. Three anatomical human body models were assumed for the computations: male and female adults, and child.

The induced electric fields by magnetic fields are computed applying the SPFD method. Besides, the 99%ile value was applied as a post-processing to reduce the stair-casing approximation error in the model. The induced electric fields by electric fields are computed applying the two-step process method combining fast-multipole surface charge and SPFD methods described in chapter 3. To speed up the method, a fast multipole method was applied.

This chapter describes the anatomical human models and computational models.

2.2. Anatomical Human Models

The Japanese adult male detailed anatomical model “TARO” and female model “HANAKO” [46] and the 3 years old child model (sex not specified) [47] developed at NICT (National Institute of Information and Communications Technology, Japan), as shown in Fig. 2.1, were used to evaluate the induced electric fields by external electric and magnetic fields. These three models were contrasted as necessary to test the effects of differences in body size due to gender and age on dosimetry results. In these models, 54 types of tissue are segmented. The voxel resolutions of the model are 2 mm for the adult models and 1 mm for the child model, respectively. TARO model is used in Chapter 3-5. HANAKO model is used in Chapter 4 and 5.

The child model is used only in Chapter 5. Specifications regarding the number of model elements are shown in Table 2.1.

The electrical conductivities of each tissue at 50 Hz used in Chapter 3 and 5 are listed in Table 2.2. These values are based on the electrical constant reported by Gabriel [48]. As shown in the table, the body part “Brain” consists of cerebellum, grey matter, hypothalamus, pineal gland, pituitary, thalamus, and white matter in our study.

In Chapter 4, the electrical conductivities of each tissue at each frequency are set based on the electrical constant database developed by IFAC (Institute of Applied Physics, a part of the Italian National Research Council, Italy) [57]. As the database offers electrical constants for frequencies of 10 Hz and over, the data at 0.153 Hz were substituted by those at 10 Hz. The electrical conductivities at 50 Hz and 1 MHz are listed in Table 2.3 as representative cases. The values of 0.1 S/m (0.153 Hz−167 Hz), 0.2 S/m (3350 Hz), 0.5 S/m (1 MHz), and 0.6 S/m (5 MHz) were assigned for skin. The composition of the body part “Brain” is similar to that of Table 2.2.

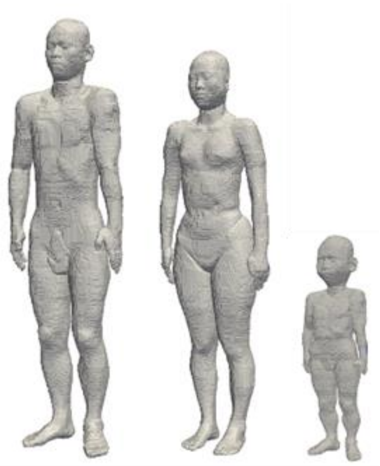

(a) (b) (c)

Figure 2.1 Anatomical models of (a) an adult male, (b) an adult female, and (c) a 3-year old child

Table 2.1 Specifications concerning the number of model elements.

Model	Voxel resolution	Total model size	Total number of effective voxels	Number of surface elements
Adult male	2 mm	320×160×866	7,977,906	713,076
Adult female	2 mm	320×160×804	6,276,179	572,449
3-year old child	1 mm	290×172×880	12,586,324	897,820

Table 2.2 Electrical Conductivities of Tissues at 50 Hz (used in Chapter 3 and 5).

Tissue type	Conductivity (S/m)	Tissue type	Conductivity (S/m)
Cerebellum *	0.10	Pancreas	0.35
CSF	2.0	Prostate	0.40
Cornea	0.40	Small intestine	0.50
Eye tissue (sclera)	1.5	Spleen	0.10
Grey matter *	0.10	Stomach	0.50
Hypothalamus*	0.080	Stomach contents	0.35
Lens	0.25	Tendon	0.30
Pineal gland *	0.080	Testis	0.35
Pituitary *	0.080	Thyroid	0.50
Salivary gland	0.35	Trachea	0.35
Thalamus *	0.080	Urine	0.70
Tongue	0.30	Air (internal)	0.0
White matter *	0.060	Blood	0.70
Adrenals	0.35	Cortical bone	0.020
Bladder	0.20	Bone marrow	0.060
Large intestine	0.10	Cartilage	0.18
Large intestine contents	0.35	Fat	0.040
Duodenum	0.50	Muscle	0.35
Esophagus	0.50	Nerve (spinal cord)	0.030
Bile	1.4	Skin	0.10
Gall bladder	0.20	Tooth	0.020
Heart	0.10	Ligament	0.30
Kidney	0.10	Small intestine contents	0.35
Liver	0.070	Diaphragm	0.35
Lung	0.14	Seminal vesicle	0.35

* indicates brain tissues (CNS tissues of the head)

Table 2.3 Electrical Conductivities of Tissues at 50 Hz and 1 MHz (used in Chapter 4).

Tissues	50 Hz	1 MHz	Tissues	50 Hz	1 MHz
Cerebellum *	0.0953	0.185	Ovary	0.321	0.358
CSF	2.00	2.00	Pancreas	0.521	0.603
Cornea	0.421	0.656	Prostate	0.421	0.562
Eye tissue (Sclera)	1.50	1.50	Small Intestine	0.522	0.865
Grey Matter *	0.0753	0.163	Spleen	0.0857	0.182
Hypothalamus*	0.0753	0.163	Stomach	0.521	0.584
Lens	0.321	0.375	Stomach Contents	0.233	0.503
Pineal Gland *	0.0753	0.163	Tendon	0.270	0.392
Pituitary *	0.0753	0.163	Testis	0.421	0.562
Salivary Gland	0.233	0.503	Thyroid	0.521	0.603
Thalamus *	0.0753	0.163	Trachea	0.301	0.373
Tongue	0.271	0.388	Urine	0.700	0.822
White Matter *	0.0533	0.102	Uterus	0.229	0.564
Adrenals	0.233	0.503	Blood	0.700	0.822
Bladder	0.205	0.236	Cortical Bone	0.0201	0.0244
Breast Fat	0.0226	0.0258	Bone Marrow	0.0412	0.0473
Large Intestine	0.0545	0.314	Cartilage	0.171	0.233
Large Intestine Contents	0.233	0.503	Fat	0.0196	0.0251
Duodenum	0.521	0.584	Muscle	0.233	0.503
Esophagus	0.521	0.584	Nerve (Spinal Cord)	0.0274	0.130
Bile	1.40	1.40	Skin	0.100	0.500
Gall Bladder	0.900	0.90	Tooth	0.0201	0.0244
Heart	0.0827	0.328	Ligament	0.270	0.392
Kidney	0.0892	0.278	Small Intestine Contents	0.233	0.503
Liver	0.0367	0.187	Diaphragm	0.233	0.503
Lung	0.137	0.235	Seminal Vesicle	0.233	0.503

* indicates brain tissues (CNS tissues of the head)

2.3. Computational Methods

2.3.1. Induced Electric Field by Magnetic Field (SPFD Method)

The internal electric fields induced in the human body were computed using the SPFD (Scalar Potential Finite Difference) method [49]. Under the quasi-static condition, electric fields can be represented as

$$\boldsymbol{E}(\boldsymbol{r}) = -j\omega\boldsymbol{A}(\boldsymbol{r}) - \nabla\phi(\boldsymbol{r}) \tag{2.1}$$

where $\boldsymbol{E}$, ω, $\boldsymbol{A}$, and ϕ are the internal electric field, angular frequency, magnetic vector potential, and electric scalar potential, respectively. Assuming a continuity condition for the current density

$$\nabla \cdot \left[\sigma(\boldsymbol{r})\boldsymbol{E}(\boldsymbol{r})\right] = 0 \tag{2.2}$$

Eq. (2.1) is reduced to the differential equation

$$-\nabla \cdot \left[\sigma(\boldsymbol{r})\nabla\phi(\boldsymbol{r})\right] = \nabla \cdot \left[j\omega\sigma(\boldsymbol{r})\boldsymbol{A}(\boldsymbol{r})\right] \tag{2.3}$$

and subject to the boundary condition

$$\sigma(\boldsymbol{r})\boldsymbol{E}(\boldsymbol{r}) \cdot \boldsymbol{n}(\boldsymbol{r}) = 0 \tag{2.4}$$

where σ is the electrical conductivity of the body tissue and $\boldsymbol{n}$ is the normal vector at the body surface. Integrating Eq. (2.3) with respect to the volume of a voxel and choosing the node of the voxel as the collocation, we derive the discretized form of the dominant equation

$$\sum_{n=1}^{6} s_n\phi_n - \left(\sum_{n=1}^{6} s_n\right)\phi_0 = j\omega\sum_{n=1}^{6}(-1)^n s_n l_n A_{0n} \tag{2.5}$$

where n denotes the index of 6 voxel nodes around the subjected node, and s_n, ϕ_n, l_n, and A_{0n} are the voxel edge conductance, electric scalar potential at a node, voxel edge length, and magnetic vector potential at the voxel edge center, respectively. Note that Eq. (2.4) is implicitly satisfied by Eq. (2.5) because $s_n = 0$ for nodes outside the model. The unknown electric scalar potentials at all the nodes are derived by solving the simultaneous equation that is formed by imposing Eq. (2.5) on all nodes. A numerical solution of this simultaneous equation was derived using the Bi-CGSTAB method [50]. Induced internal electric fields are derived from the gradient of the electric scalar potential by taking the difference between values at two adjacent nodes on the voxel edge. The induced electric field value at the voxel center was derived by taking the average of the values at four parallel edge centers.

2.3.2. Post-processing Algorithm

In computational dosimetry, the stair-casing approximation of voxel human model may result in a significant error if pre-/post-processing is not appropriately performed [51], [52]. In this thesis, the 99%ile value, which is defined in ICNIRP guideline [9] is employed as the maximal value of the induced electric field.

2.3.3. Speeding Up of Computational Process (Fast-Multipole Method)

The fast-multipole method (FMM) [58] is a computational method that can evaluate Coulomb-type interaction computations for many-body particle systems with a computational complexity of O (N), which originally required $O(N^2)$. It has been applied in various fields dealing with many-body systems, such as astrophysics [59] and molecular dynamics calculations [60], and has also been applied in the field of electromagnetic field analysis [61] ~ [64]. FMM is used to speed up matrix-vector product operations in Chapter 3.

In FMM, a hierarchical nested structure of rectangular cells is defined to encompass the elements (particles) to be computed for the interaction. The processing procedure of FMM consists of two processes: Upward Pass, in which multipole expansion coefficients are computed from the leaf cell to the root cell, and Downward Pass, in which local expansion coefficients are computed from the root cell to the cells in the lower hierarchical levels. In Upward Pass, the multipole expansion factor M_n^m is first computed for a leaf cell by the following equation.

$$M_n^m = \sum_{i=1}^{k} q_i \rho_i^n Y_n^{-m}(\alpha_i, \beta_i) \tag{2.6}$$

where q_i is the total charge (i = 1, 2, ..., k) contained in the leaf cell, (ρ_i, α_i, β_i) are the polar coordinates of element i measured from the leaf cell center, and Y_n^{-m} is the spherical harmonic function. Next, the multipole expansion coefficients of the leaf cell (A) are transformed and added according to the following formula to compute the multipole expansion coefficients of the cell one above (B) (M2M transformation).

$$M^{(B)}{}_{l}^{s} = \sum_{n=0}^{l} \sum_{m=-n}^{n} \frac{M^{(A)}{}_{l-n}^{s-m} \, j^{|s|-|m|-|s-m|} A_n^m A_{l-n}^{s-m} \rho^n Y_n^{-m}(\alpha, \beta)}{A_l^s} \tag{2.7}$$

where $A_n{}^m$ is expressed as

$$A_n^m = \frac{(-1)^n}{\sqrt{(n-m)!(n+m)!}} \tag{2.8}$$

Here, (ρ, α, β) are the polar coordinates of the center of gravity of the destination cell B with respect to the center of gravity of the source cell A. The definition is the same for the following various transformation operations: By performing M2M transformation up to the root cell and then up the hierarchy, the multipole expansion coefficients for all hierarchical cells can be computed.

In Downward Pass, local expansion coefficients can be defined for cells in all layers by performing the operation of converting multipole expansion coefficients of a child cell (A) in a neighboring cell of the parent cell that is not adjacent to its own cell (B) to local expansion coefficients (M2L transformation, eq. (2.9)) and also by performing the operation of converting local expansion coefficients of the parent cell (A) to local expansion contributions of the child cell (B) (L2L transformation, eq. (2.10)).

$$L^{(B)}{}_{l}^{k} = \sum_{n=0}^{p} \sum_{m=-n}^{n} \frac{M^{(A)}{}_{n}^{m} \, j^{|k-m|-|k|-|m|} A_n^m A_l^k \rho^n Y_{l+n}^{m-k}(\alpha, \beta)}{(-1)^n A_{l+n}^{m-k} \rho^{l+n+1}} \tag{2.9}$$

$$L^{(B)}{}_{l}^{k} = \sum_{n=l}^{p} \sum_{m=-n}^{n} \frac{L^{(A)}{}_{n}^{m} \, j^{|m|-|m-k|-|k|} A_{n-l}^{m-k} A_l^k \rho^{n-l} Y_{n-l}^{m-k}(\alpha, \beta)}{(-1)^{n+l} A_n^m} \tag{2.10}$$

where p is the censoring order of the local expansion, and the larger p, the better the accuracy of the approximation.

Finally, the local expansion coefficients of the leaf cells are used to compute the contribution of the interaction from all elements except the elements of its own cell and its neighboring cells by the following formula.

$$\phi = \sum_{n=0}^{p} \sum_{m=-n}^{n} L_n^m r^n Y_n^m(\theta, \phi) \tag{2.11}$$

The interaction by the elements in its own cell and adjacent cells is not included in the local expansion coefficients, so it is computed directly. In this way, the interaction computation is performed hierarchically, and finally the interactions by all elements other than the own cell and adjacent cells are included in the local coefficients, which reduces the amount of computation for the interaction computation between N bodies, which originally requires $O(N^2)$, to $O(N)$.

Chapter 3

Development of Two-Step Process Method of Dosimetry Under ELF Electric Field Exposure Combining Fast-Multipole Surface Charge and SPFD Methods

3.1. Overview

This chapter proposes a two-step process method combining the fast-multipole surface charge and SPFD methods to evaluate the electric field induced in human body exposed to ELF electric field. The proposed method was applied to a comprehensive anatomical human model to derive the internal electric field induced by external ELF electric field. Because the proposed method does not need to take any electric quantity into account outside the body, it saves a considerable amount of memory and computation time, as compared with the QS-FDTD method that is frequently used in previous studies.

The results presented here were published in [72].

3.2. Proposed Method

3.2.1. Overview of Proposed Method

The surface of the human body exposed to a low-frequency electric field induces a surface charge that cancels out the external electric field, and a capacitive current flows inside the body driven by the fluctuation of the surface charge, resulting in an electric field inside the body [13]. The proposed method consists of two steps, the surface charge method and the SPFD method [49], corresponding to these two-step processes. Fig. 3.1 shows a schematic diagram of the proposed method. In the first step, the surface charge induced on the human body surface is computed by the surface charge method. In the second step, the induced electric field in the body is computed by the SPFD method using the surface charge as the source term.

The governing equations of the surface charge method are $N \times N$ dense matrices (N is the total number of elements on the surface of the human body model) because they are composed of many-body interactions among all surface elements. As described in Section 3.3, for a detailed anatomical human body model with a resolution of several millimeters, N can be as large as several hundred thousand, which involves an enormous computational load. To solve this problem, the proposed method incorporates the fast multipole method into the surface charge method to significantly reduce this computational load. In the following sections, we describe the details of the surface charge method, the fast multipole method, and the SPFD method, respectively.

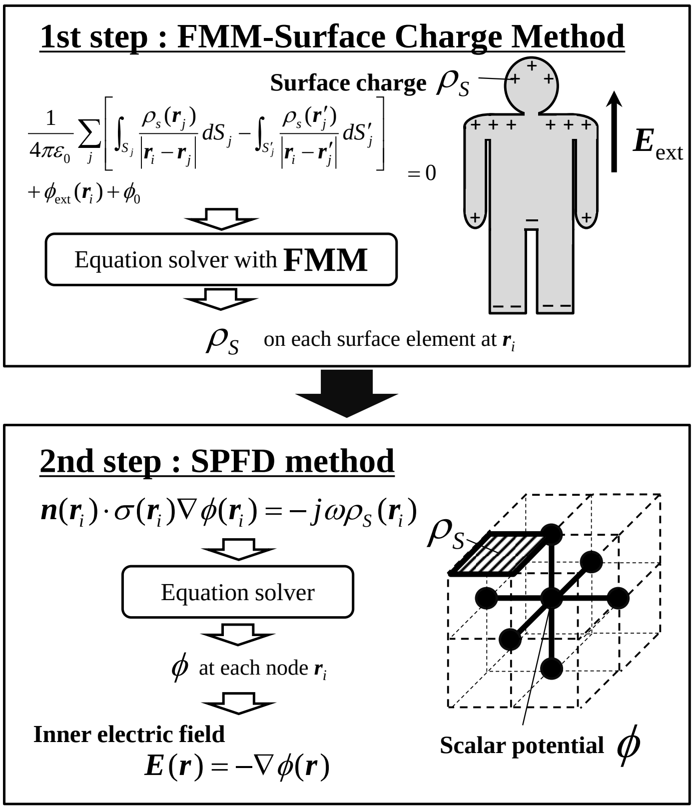

Figure 3.1 Schematic diagram of the proposed method.

3.2.2. 1st Step: Surface Charge Method

The proposed method first computes the surface charge induced on the surface of the human body by the electric field. The following integral equation is derived from the condition that the electric field inside the body created by the surface charge cancels the external electric field [13].

$$\frac{1}{4\pi\varepsilon_0}\sum_{j=1}^{N}\left[\int_{S_j}\frac{\rho_s(\boldsymbol{q}_j)}{|\boldsymbol{r}_i-\boldsymbol{q}_j|}dS_j-\int_{S'_j}\frac{\rho_s(\boldsymbol{q}'_j)}{|\boldsymbol{r}_i-\boldsymbol{q}'_j|}dS'_j\right]+\phi_{\text{ext}}(\boldsymbol{r}_i)+\phi_0=0 \qquad (3.1)$$

where $\boldsymbol{r}_i$ is the center location of discretized surface elements, S_j is the integral area of surface elements, $\boldsymbol{q}_i$ is the position vector in surface element, ϕ_{ext} is the electric scalar potential due to external electric field and given by $\phi_{ext}(\boldsymbol{r}) = -\boldsymbol{E}_{ext}\cdot\boldsymbol{r}$ in the case of uniform external electric field $\boldsymbol{E}_{ext}$, ϕ_0 is the reference value for electric scalar potential, ρ_s is the surface charge density, and N is the number of surface elements. The first and second terms in brackets "[ ]" within Eq. (3.1) represent the Coulomb potential due to the other charge elements and the contribution to the Coulomb potential due to the shadow charge elements, respectively. The latter accounts for the earth's conduction effects and is not necessary when dealing with exposure to electric fields under conditions in which the human body can be considered to be placed in free space (hereinafter referred to as "free space conditions"). In the proposed method, the center of the surface element is assumed to be the collocation, and the surface charge is assumed to be constant on the element, henceforth, $\rho_s(\boldsymbol{r}_i) = \rho_s^{(i)}$. Based on this, equation (3.1) is formulated for all elements $\boldsymbol{r}_i$ (i = 1, 2, ..., N) to derive the following simultaneous equations.

$$\begin{bmatrix} M_{11} & M_{12} & \cdots & M_{1N} \\ M_{21} & M_{22} & \cdots & M_{2N} \\ \vdots & \vdots & \ddots & \vdots \\ M_{N1} & M_{N2} & \cdots & M_{NN} \end{bmatrix} \begin{Bmatrix} \rho_S^{(1)} \\ \rho_S^{(2)} \\ \vdots \\ \rho_S^{(N)} \end{Bmatrix} = - \begin{Bmatrix} \phi_{\text{ext}}(\boldsymbol{r}_1) + \phi_0 \\ \phi_{\text{ext}}(\boldsymbol{r}_2) + \phi_0 \\ \vdots \\ \phi_{\text{ext}}(\boldsymbol{r}_N) + \phi_0 \end{Bmatrix} \tag{3.2}$$

Here, M_{ij} is given by following equation.

$$M_{ij} = \frac{1}{4\pi\varepsilon_0}\left[\int_{S_j} \frac{dS_j}{\left|\boldsymbol{r}_i - \boldsymbol{q}_j\right|} - \int_{S'_j} \frac{dS'_j}{\left|\boldsymbol{r}_i - \boldsymbol{q}'_j\right|}\right] \tag{3.3}$$

In the free-space condition or the condition where the body is suspended to the ground and there is no electrical contact (hereinafter referred to as the floating condition), the following equation is valid because the total charge on the body surface is conserved.

$$\rho_S^{(1)}\Delta S_1 + \rho_S^{(2)}\Delta S_2 + \cdots + \rho_S^{(N)}\Delta S_N = 0 \tag{3.4}$$

Here, ΔS_i represents the area of the i-th surface element, but in the case of voxels, ΔS_i is constant for all elements, so it can be divided from equation (3.4) to derive

$$\rho_S^{(1)} + \rho_S^{(2)} + \cdots + \rho_S^{(N)} = 0 \tag{3.5}$$

By combining equations (3.5) and (3.2), the following equation is derived.

$$
\begin{bmatrix} M_{11}-M_{N1} & M_{12}-M_{N2} & \cdots & M_{1N}-M_{NN} \\ M_{21}-M_{N1} & M_{22}-M_{N2} & \cdots & M_{2N}-M_{NN} \\ \vdots & \vdots & \ddots & \vdots \\ 1 & 1 & \cdots & 1 \end{bmatrix} \begin{Bmatrix} \rho_S^{(1)} \\ \rho_S^{(2)} \\ \vdots \\ \rho_S^{(N)} \end{Bmatrix} = -\begin{Bmatrix} \phi_{\mathrm{ext}}(\boldsymbol{r}_1)-\phi_{\mathrm{ext}}(\boldsymbol{r}_N) \\ \phi_{\mathrm{ext}}(\boldsymbol{r}_2)-\phi_{\mathrm{ext}}(\boldsymbol{r}_N) \\ \vdots \\ 0 \end{Bmatrix} \tag{3.6}
$$

The unknown number $\rho_s^{(i)}$ is derived by solving equation (3.6) numerically. Note that equation (3.5) is not necessary when the human body is grounded, so equation (3.2) can be constructed and solved after excluding the surface elements on the ground plane. As can be seen from Eqs. (3.2)–(3.6), the coefficient matrix of the governing equations of the surface charge method is a dense matrix with $N \times N$ elements and is asymmetric. For this reason, the Bi-CGSTAB method [50], which is one of the methods applicable to asymmetric and dense matrices, was applied as a numerical solution method for the governing equations. When the coefficient matrix is a dense matrix, an iterative solution method such as the Bi-CGSTAB method requires an order $O(N^2)$ of operations to compute the matrix-vector product per step. In the detailed anatomical human body model [46], which is the subject of this study, N is several hundred thousand, so the computational load is enormous. Therefore, we applied the fast multipole method to reduce the computational load of the matrix-vector product. The details of the application of the fast multipole method are described in the next section.

3.2.3. Speeding Up of Solution Process Applying FMM

The FMM described in Section 2.3.3 is applied to speed up the solution process of the surface charge method. As described in the previous section, when the Bi-CGSTAB method is applied to solve equations (3.2) or (3.6), the computation of the matrix-vector product per step requires $O(N^2)$ operations, but by applying FMM, this load is reduced to $O(N)$. In incorporating FMM into the surface charge method, the following points (1) and (2) were taken into account, referring to previous studies [61] ~ [65].

(1) Computation of Shadow Charge Contribution

The contribution from the shadow charge was taken into account by assuming a cell structure in the shadow image region as well and adding the local expansion coefficients of the shadow image region as a target during the M2L transform, as described in ref. [64]. The local expansion coefficients of the shadow image part do not need to be computed anew, but can be computed by the following equation for the local expansion coefficient M of the real image, using the symmetry of the spherical harmonic function.

$$M'^{m}_{n} = (-1)^{|m|+n} M^{m}_{n} \tag{3.7}$$

Note that the bottom surface of the root cell is defined to be tangent to the earth to prevent leaf cells containing charges in the vicinity of the earth from crossing over the earth. In this case, for the leaf cell that is tangent to the earth, in addition to the M2L transformation described above, the direct computation contribution by the elements in the neighboring cells in the shadow side region of the cell must also be added.

(2) Speeding Up of Direct Computation Part

In FMM, the effect of distant elements is taken into account through local expansion coefficients, but the effect of elements belonging to adjacent leaf cells must be evaluated by direct computation [58], [64], [65]. Therefore, it is also important to speed up the direct-computation part. The proposed method, based on Hamada et al.'s method [63], uses the characteristic of voxels that the centers of surface elements are arranged in a grid pattern to precompute the direct-computation part and retain the results as a three-dimensional array, thereby significantly reducing the computational load on the direct-computation part. Since the area requiring direct computation is up to the adjacent leaf cells, the array size to hold the pre-computed results is only a few dozen per dimension at most when the leaf cells are about 10 voxels per side, as in the computational conditions in this study.

As shown in Appendix A, the speed-up effect of the matrix-vector product computation when FMM is applied compared to when FMM is not applied is about 60 times faster for the scale of the detailed human body model used in this study (N = 700,000 or so). Since the M2L transformation generally has a large load and becomes a bottleneck in the fast multipole method, there are reports that the load is greatly reduced by applying a rotational transformation of the coordinate axes or a diagonalization transformation using exponential expansion to the M2L computation process [63], [64].

3.2.4. 2nd Step: SPFD method

The SPFD method computes the induced electric field in the body by solving the difference equation with the electric scalar potential as the unknown and taking the gradient of the derived electric scalar potential [49]. Other applications than electric field exposure have been reported, such as the computation of induced electric fields due to magnetic field exposure with the source term as a vector potential [16], [17], [24], [49] and the computation of currents in a body with the contact current of a charged object as a source term [66], [67]. In the proposed method, the surface charge ρ_s derived by solving Eqs. (3.2) or (3.6) is treated as the source term.

According to the conservation law of current density, the following boundary condition is established at the surface of the human body.

$$\boldsymbol{n}(\boldsymbol{r}) \cdot \sigma(\boldsymbol{r}) \nabla \phi(\boldsymbol{r}) = -j\omega\rho_S(\boldsymbol{r}) \tag{3.8}$$

In addition, the following differential equation holds inside the body

$$\nabla \cdot \left[\sigma(\boldsymbol{r}) \nabla \phi(\boldsymbol{r})\right] = 0 \tag{3.9}$$

where σ is the conductivity and ϕ is the electric scalar potential. By discretizing equations (3.8) and (3.9) with the voxel vertex position as the defining point of the electric scalar potential, the following equation is derived.

$$\sum_{n=1}^{6} s_{I(i,n)}\phi_{I(i,n)} - \left(\sum_{n=1}^{6} s_{I(i,n)}\right)\phi_i = -\frac{j\omega\Delta L^2}{4}\sum_{m=1}^{12}\rho_S^{(J(i,m))} \tag{3.10}$$

where ϕ_i: the electric scalar potential of node i, $I(i, n)$: the index of the adjacent nodes of node i (n = 1, 2, ..., 6 correspond to the left, right, front, back, top and bottom neighbors of node i, respectively), $S_{I(i,\,n)}$: the conductance between adjacent nodes, ΔL: the size of one side of a voxel, $J\,(i, m)$: the index (m = 1, 2, ..., 12) of the 12 sides sharing node i. In implementing the program, it is possible to consider both equations (3.8) and (3.9) in equation (3.10) alone by defining array variables so that $\rho_s\,(J\,(i, m)) = 0$ if the side pointed to by the index $J\,(i, m)$ does not contain any nodes on the surface. The electric scalar potential is derived by solving a simultaneous linear equation consisting of equation (3.10) for all nodes (i = 1, 2, ..., N'). The gradient of the electric scalar potential yields the induced electric field in the body. In other words, as shown in the following equation for the x component of the electric field, the electric field at their midpoint can be derived by the difference between adjacent nodes (the same concept applies to the y and z components).

$$E_x(i+1/2, j, k) = -\frac{\phi(i+1, j, k) - \phi(i, j, k)}{\Delta L} \tag{3.11}$$

where (i, j, k) are the lattice coordinates with the voxel vertices as lattice points. The average of the electric fields at the midpoints of the four parallel sides of a voxel, derived by Eq. (3.11), gives the electric field at the center of the voxel (hereafter, the voxel's electric field). Since equation (3.8) is a Neumann boundary condition, the potential reference may be undefined if only equation (3.10) is used. Therefore, as a Dirichlet boundary condition, we apply the condition that the average potential in the body is zero under the free space condition or the floating condition, as shown in the following equation.

$$\phi_1 + \phi_2 + \cdots + \phi_{N'} = 0 \tag{3.12}$$

In the grounding condition, this equation is no longer necessary, and instead, the condition that the potential of the nodes on the ground plane is 0 is applied. By incorporating the condition in equation (3.12), the coefficients of the simultaneous equations become an asymmetric matrix.

Therefore, the Bi-CGSTAB method is applied to the SPFD method as well as the surface charge method to solve the governing equations.

3.3. Verification of Proposed Method Using Anatomical Human Model

3.3.1. Common Computational Conditions

The proposed method was applied to compute the induced electric field in the body under the vertical uniform electric field exposure condition (50 Hz) using a detailed anatomical human body model. The validity of the proposed method was verified by comparison with the conventional quasi-static finite difference time domain (QS-FDTD) method (Appendix B). The model for the computations was the adult male model TARO, described in detail in Section 2.2. Two types of exposure conditions to the electric field were assumed: free-space conditions and a case in which the earth was considered. The electric field was assumed to be a vertical, spatially uniform, AC electric field with an intensity of 1 kV/m and a frequency of 50 Hz. In the following figures, X, Y, and Z are defined as the left-right, front-back, and height directions of the human body, respectively.

Iterative modification of the solutions by the Bi-CGSTAB method for the surface charge and SPFD methods was performed until the residuals of the simultaneous equations $||\boldsymbol{b} - A\boldsymbol{x}||/||\boldsymbol{b}||$ (where $||\ ||$ is the 2-norm of the vector) were 10^{-8} and 5×10^{-6}, respectively. The leaf cell of the FMM was a cubic region made of 10 × 10 × 10 voxels, and the censoring order p of the multipole expansion was set to 6. The value of p was determined by prior verification so that the error of the matrix vector product computation when FMM is applied relative to when FMM is not applied (i.e., $||\boldsymbol{b}_2 - \boldsymbol{b}_1|| / ||\boldsymbol{b}_1||$ where $\boldsymbol{b}_1$ is the matrix vector product derived by direct computation without FMM and $\boldsymbol{b}_2$ is that with FMM) is less than 1/1000 %.

For the QS-FDTD computations, 16 layers of PML absorbing boundaries were used, and a separation of 6.4 cm (32 voxels) was maintained between the PML absorbing boundaries and the human body model to further reduce the influence of reflected waves. Iterative updates of the electromagnetic field were performed until the relative change per step in the electric field in the body was less than 10^{-6} of the value of the previous step.

3.3.2. Induced Electric Field Under Free-space Conditions

Fig. 3.2 shows the spatial distribution of surface charge density derived by the proposed method under free-space conditions. The figure shows that positive charge densities are observed on the head and shoulders, while negative charge densities are conspicuously distributed on other parts of the body. Fig. 3.3 (a) shows the distribution of the induced electric field strength in the body in a cross section near the center of the human body model in the Y direction (cross section near Y = 0.9 cm when the Y direction of the model domain is assigned to −15.9 cm ~ 15.9 cm) derived by the proposed method. Fig. 3.3 (b) shows the average value of the induced electric field intensity in each horizontal cross section in the height direction. In addition, Table 3.1 shows the average, maximum, and 99th percentile values (99 % value) for brain tissue, spinal cord, and whole body, based on the evaluation method described in Section 2.3.2.

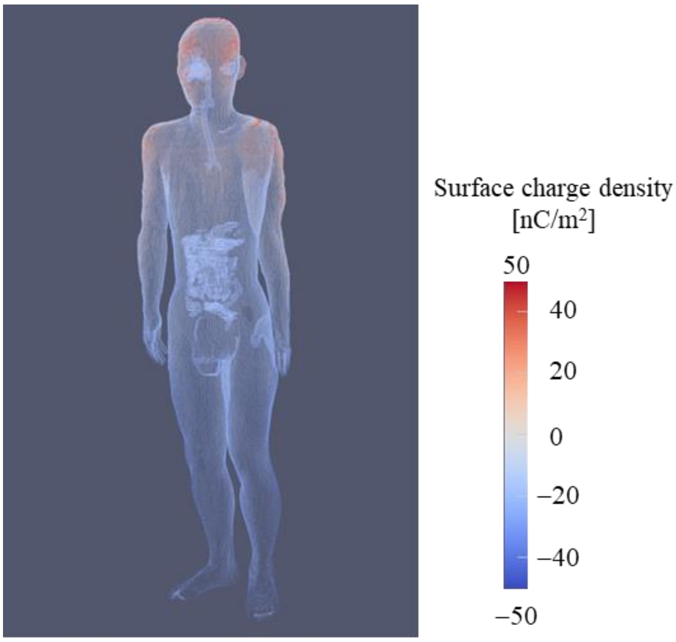

Figure 3.2 Spatial distribution of surface charge density.

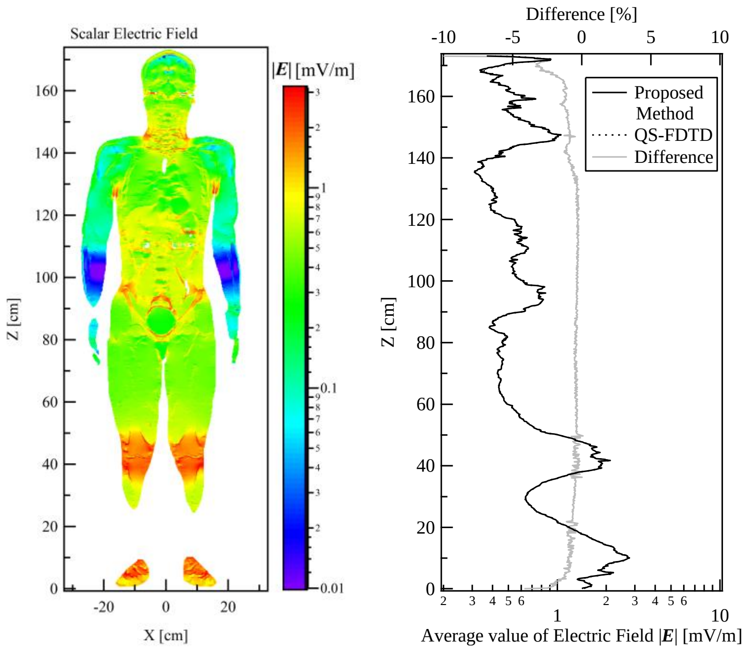

(a) (b)

Figure 3.3 Computational results of inner electric field induced by vertical electric field (50 Hz, 1 kV/m) in free space. (a) Distribution of induced inner electric field at cross section (Y = 0.9 cm), (b) Vertical distribution of average value of induced inner electric field strength in each Z cross section.

Table 3.1 Average, maximum, and 99th percentile values of induced electric field strength |***E***| (mV/m) in the brain, the spinal cord, and whole body.

Tissue	Statistics	Proposed method	QS-FDTD	Difference
Brain	Average	0.406	0.411	-1.22 %
	Max	2.15	2.17	-0.92 %
	99^{th} %ile	0.983	0.993	-1.01 %
Spinal cord	Average	0.684	0.688	-0.58 %
	Max	5.40	5.43	-0.55 %
	99^{th} %ile	2.19	2.21	-0.90 %
Whole body	Average	0.622	0.626	-0.64 %
	Max	7.59	7.67	-1.04 %
	99^{th} %ile	2.16	2.18	-0.92 %

Fig. 3.3 (b) and Table 3.1 also show the results of computations under the same conditions using the QS- FDTD method in addition to the proposed method for comparison. In the same figure and table, the difference between the proposed method and the QS-FDTD method (= [(proposed method)-(QS-FDTD method)]/(QS-FDTD method)) is also shown.

As shown in Fig. 3.3 (a), (b), the induced electric field strength is characterized by an increase in the electric field strength at locations with a small horizontal cross-sectional area, such as near the knees and ankles. This is considered to be because, as is well known, under the exposure conditions of the present study, the electric current mainly flows in the direction of height, and the electric current is concentrated in areas with small cross-sectional areas, and the electric field is increased accordingly. Fig. 3.3 (b) shows that the proposed method evaluates 0.2 % to 10 % smaller than the QS-FDTD method for the average value in each horizontal cross section, although it is difficult to distinguish the difference visually because the results of them almost overlap at the waveform level. In addition, Table 3.1 shows that the proposed method evaluates the 99 % value of the electric field in each tissue to be 1.22 % smaller than the QS-FDTD method at the maximum. The reason why the proposed method evaluates the electric field smaller than the QS-FDTD method is considered to be the effect of small reflected waves at the PML absorption boundary in the computation by the QS-FDTD method. In other words, it is thought that the residual reflected waves in the computational space increase the effective external electric field, and thus the induced electric field in the body is evaluated to be larger. In Fig. 3.3 (b), the differences in the averaged values within each horizontal section are larger near the top of the head (around Z = 173 cm) and near the soles of the feet (Z = 0 cm). This may be due to the fact that the PML absorbing boundary is significantly less effective for electromagnetic fields whose incident direction is parallel to the boundary plane [54]. Note that the Berenger's PML absorption boundary [55] was used in this study, and the absorption performance for the horizontal incident component is low. Specifically, it is considered that the PML absorption boundary facing the top of the head and the soles of the feet is less effective because the external electric field in the Z direction is dominant under the present computational conditions. This is also consistent with the above speculation that the reflected wave at the PML absorption boundary is the reason for the difference from the proposed method.

3.3.3. Induced Electric Field Under Consideration of the Ground

For more realistic conditions, computations were performed under the condition of a perfectly conductive ground. There were two analysis cases: one in which the soles of the feet were floating by 1 cm above the ground (hereafter referred to as the “floating by 1cm” condition) and the other in which both feet were grounded (hereafter referred to as the “grounded by both feet” condition). The floating by 1cm and grounded by both feet conditions were assumed for the case of wearing shoes and standing upright on the ground in a wet condition, respectively.

Fig. 3.4 shows the distribution of the induced electric field strength in the body derived by the proposed method under the conditions of floating by 1cm and grounded by both feet (the position of the cross section is the same as in Fig. 3.3 (a)). Fig. 3.5 shows the average strength of the induced electric field in the body in each horizontal cross section in the direction of body height. Table 3.2 shows various statistics as in Table 3.1 for the brain, spinal cord, and whole body.

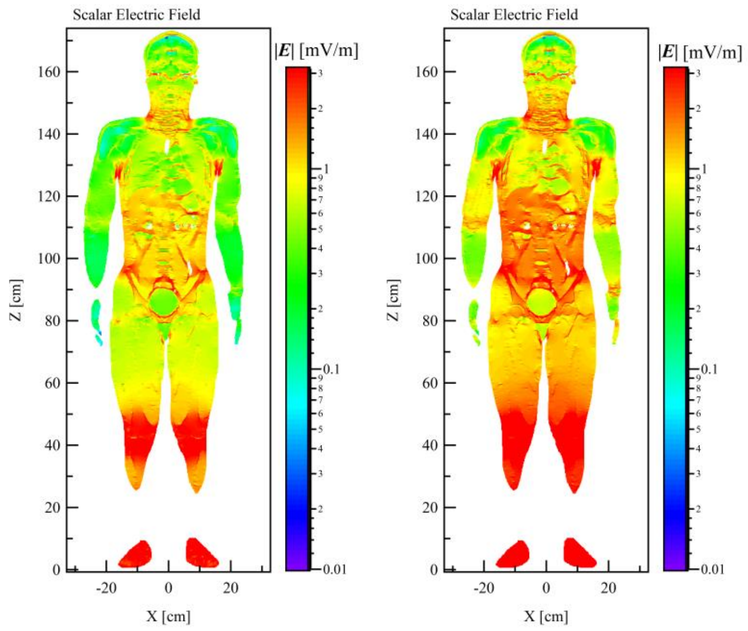

(a) (b)

Figure 3.4 Distribution of induced electric field at cross section (Y = 0.9 cm) induced by vertical electric field (50 Hz, 1 kV/m) under (a) floating by 1cm and (b) grounded by both feet conditions derived by proposed method.

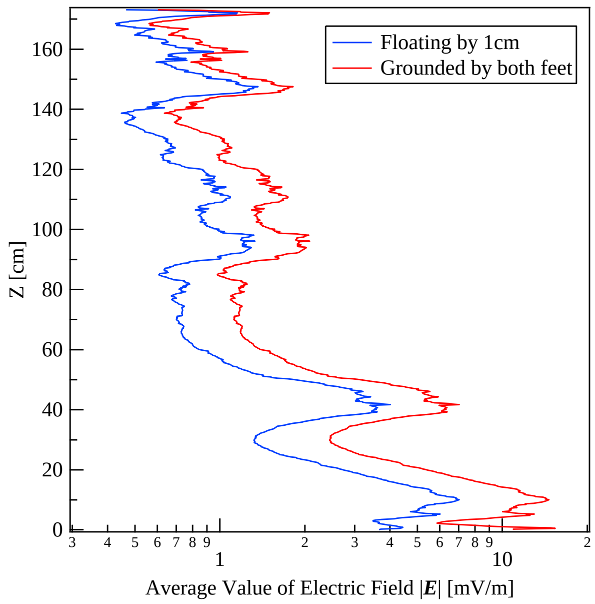

Figure 3.5 Vertical distribution of average value of induced inner electric field strength in each Z cross section with perfect conducting ground.

Table 3.2 Average, maximum, and 99th percentile values of induced electric field strength |***E***| (mV/m) in the brain, the spinal cord, and whole body.

Tissue	Statistics	Floating by 1cm		Grounded by both feet	
		Proposed method	QS-FDTD	Proposed method	QS-FDTD
Brain	Average	0.520	0.446	0.685	0.475
	Max	2.75	2.36	3.61	2.51
	99th %ile	1.26	1.08	1.66	1.15
Spinal cord	Average	0.952	0.770	1.35	0.861
	Max	7.42	6.06	10.4	6.71
	99th %ile	3.09	2.47	4.50	2.78
Whole body	Average	1.10	0.787	1.87	0.997
	Max	20.1	12.9	63.5	29.1
	99th %ile	4.98	3.26	11.0	5.10

Fig. 3.3 to Fig. 3.5, Table 3.1 and Table 3.2 show that the electric field strength increases in the order of the grounded by both feet condition, the floating by 1cm condition, and the free-space condition. This is thought to be due to the fact that the closer the distance between the ground and the human body, the greater the attraction between the surface charge and the shadow charge, and the greater the induced surface charge. In addition, the induced electric field in the body by the proposed method is larger than that by the QS-FDTD method under the conditions of grounded by both feet and floating by 1cm. The reasons for this are examined in the next section.

3.4. Performance Evaluation of Proposed Method in Comparison with Conventional Method

The effectiveness of the proposed method in reducing the computational load is verified through a comparison with the conventional QS-FDTD method. It has been reported that the distance between the absorbing boundary and the target (i.e., the size of the analysis space) affects the computational accuracy of the QS-FDTD method [34], [68]. Therefore, prior to the comparative study, we verified the correlation between the size of the analysis space and the intensity of the induced electric field in the body using the QS-FDTD method.

As shown in Fig. 3.6 (a), the separation *d* between the space occupied by the human model and the PML absorption boundary was set from 6.4 cm to 224 cm. To reduce the computational load, a human model with a reduced resolution of 8 mm (total number of voxels: 80 × 40 × 216), which is one-fourth of the original model, was used in this study (hereinafter referred to as “1/4 reduced model”) because the computational load on the full model is enormous.

Fig. 3.6 (a) shows the averaged values of the induced electric field strength in the body in each horizontal section in the height direction. Fig. (b) plots the difference between the results derived by the QS-FDTD method and those derived by the proposed method in (a) (i.e., $\| \boldsymbol{E}_2 - \boldsymbol{E}_1 \| / \| \boldsymbol{E}_1 \|$ when the former is $\boldsymbol{E}_2$ and the latter is $\boldsymbol{E}_1$) as a function of separation d.

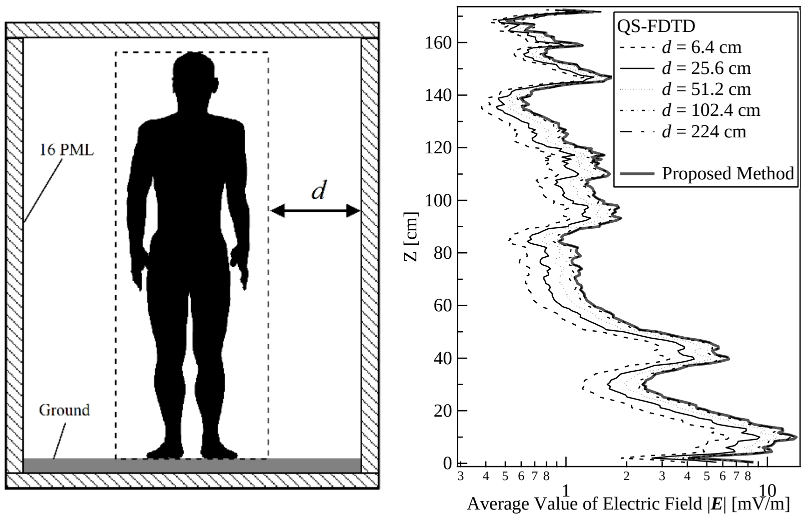

(a)

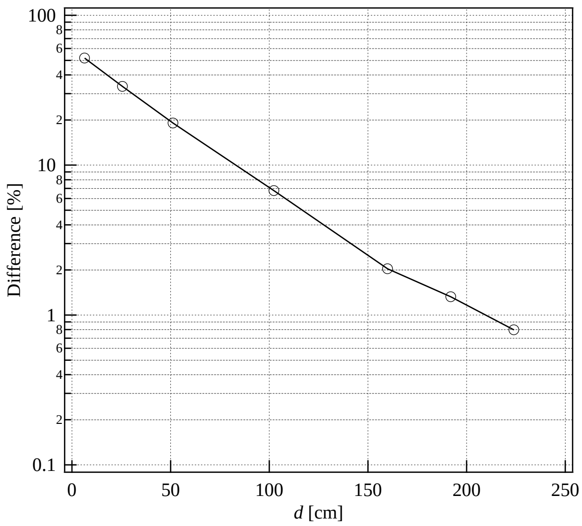

(b)

Figure 3.6 Relationship between the distance to PML boundary *d* and vertical distribution of inner electric field in QS-FDTD method using a human model of 1/4 resolution (80×40×216). (a) Vertical distribution of average value of induced electric field strength in each Z cross section. (b) Difference of average value of induced electric field between proposed method and QS-FDTD method.

As seen in Fig. 3.6 (a) and (b), the difference between the QS-FDTD method and the proposed method decreases with increasing separation *d*, and at *d* = 224 cm the results agree with those of the proposed method within 1 %. Note from Table 3.1 that the difference between the QS-FDTD method with absorbing boundaries and the proposed method is approximately 1%. This indicates that the proposed method more accurately simulates the effects of shadow charges and evaluates induced electric fields more correctly than the QS-FDTD method because the proposed method strictly simulates an infinite conductor ground, while the QS-FDTD method has a finite ground size.

Based on the results above, a comparison of the computational load of the proposed method and the QS-FDTD method is presented. Table 3.3 compares the memory consumption and computation time for the proposed method and the QS-FDTD method. Only the computational load of the QS- FDTD method for the case of grounded by both feet is estimated from the results of the 1/4 reduced model, while the other values are those of the full model. All computations in this section were performed on a personal computer equipped with an intel® core™ i7 CPU (8 cores) with a clock frequency of 4 GHz and 32 GB of RAM. In all cases, single-core computations were performed without parallel computing.

In the case of the free-space condition, the QS-FDTD method consumed 8.4 GB of memory and 46.9 hours of computation time, while the proposed method consumed 1.2 GB-3.3 GB and 8.6 hours, respectively, which means that the memory consumption and computation time were reduced by about 39 % and 18 %, respectively, compared to the QS-FDTD method. The first stage of the proposed method, the fast multipole surface charge method, takes 7.3 hours,

Table 3.3 Comparison of computational cost between proposed method and QS-FDTD method.

Method	Condition	Memory consumption	Computation time
Proposed method	Free space	1.2 GB (FMM-SCM), 3.3 GB (SPFD)	7.3 H (FMM-SCM) + 1.3 H (SPFD)
	Grounded by both feet	1.2 GB (FMM-SCM), 3.3 GB (SPFD)	6.6 H (FMM-SCM) + 1.3 H (SPFD)
QS-FDTD	Free space	8.4 GB	46.9 H
	Grounded by both feet	486.7 GB *	332.8 H *

* Estimates from the result of 1/4 resolution model

accounting for about 84% of the total computation time. The number of iterations required to solve the fast multipole surface charge method and the SPFD method under free-space conditions was 113 and 2898, respectively, indicating that the time required per iteration was 233 and 1.6 seconds, respectively. This result clearly suggests that the rate of execution of the fast multipole surface charge method is the rate-limiting factor. Further speed-up of FMM is desired in the future by applying rotational transformation of coordinate axes and diagonalization transformation by exponential expansion [63], [64]. For the case of the grounded by both feet condition, the proposed method consumes the same amount of memory as the case of the free-space condition, and the computation time is also reduced by 0.7 hours. On the other hand, the QS-FDTD method is estimated to require about 147 times more memory and about 42 times more computation time than the proposed method (that means about 0.68 % and 2.4 % reduction of computational load, respectively), based on the results for a 1/4 reduced model. This is because, as mentioned earlier, the QS-FDTD method requires a large enough analysis space to accurately account for the effects of conductor ground. These results show the superiority of the proposed method over the QS-FDTD method in terms of computational load.

The other previous method, the SPFD-based method [37] ~ [39] by Tarao et al. could not be directly compared here because we did not create a program using this method in this study. Here, we infer the difference in memory consumption from the proposed method based on the scale of the computational model described in the literature. Ref. [39] performed computations using the same model and under the same conditions as the present study (human body upright and grounded, 50 Hz, 1 kV/m uniform electric field exposure) and reported that the total number of voxels in the analysis domain was 60 to 100 million. Although the memory consumption depends on the implementation of the program and cannot be compared in general, the proposed method requires, at most, about 8 million voxels in the body, whereas the method of Tarao et al. requires at least 60 million voxels. Therefore, as a rough estimate, the proposed method is expected to reduce memory by a factor of 7.5 (8 million/60 million).

In addition, as mentioned earlier, this study does not incorporate parallel computing methods for the program, but parallel computing methods such as OpenMP and GPGPU may be applied to further reduce the computation time required.

3.5. Conclusion

This Chapter proposed a two-step method for analyzing induced electric fields in a body using the surface charge method and the SPFD method. The surface charge method is implemented with the fast multipole method to reduce the computational load and make it a practical method.

The proposed method is applied to a detailed anatomical human body model to evaluate the induced electric field in the body under low-frequency electric field exposure conditions. The results were compared with those of the QS-FDTD method under free-space conditions, and it was confirmed that the results generally agreed well with those of the QS-FDTD method, but it was suggested that the QS-FDTD method evaluated the induced electric field in the body larger than the proposed method due to the effect of reflected waves at the PML absorption boundary. Compared to the QS-FDTD method, the proposed method consumes about 0.68% (both feet on the ground condition) to 39% (free space condition) less memory and takes about 2.4% (both feet on the ground condition) to 18% (free space condition) less computation time, indicating that the proposed method is practical. Furthermore, the proposed method simulates the effect of shadow charge more accurately than the QS-FDTD method, and can evaluate the induced electric field more correctly. In this chapter, we have evaluated the method for exposure to uniform electric fields, but in the future, we plan to evaluate the method under non-uniform field exposure conditions and with other models. Another issue to be addressed is to reduce the computational load by further increasing the speed of the fast multipole surface charge method.

Chapter 4

Dosimetry of Internal Electric Fields Induced by ELF and Intermediate Frequency Uniform Magnetic Fields at Reference Level of IEEE C95.1^{TM}-2019 Standard

4.1. Overview

In this Chapter, the internal electric field induced in human tissues by ELF and intermediate frequency uniform magnetic fields has been determined using the SPFD method. These computations were conducted on adult Japanese anatomical models and the computational results were compared with the basic restriction provided in the IEEE safety standard. Under the reference levels condition defined in the IEEE C95.1^{TM}-2019 standard, the computed internal electric fields exceeded the basic restriction in the cases for certain body parts and conditions.

The results presented here were published in [73].

4.2. Computational Conditions

4.2.1. Exposure Scenarios

Three orientations were assumed for the magnetic field; LAT (side-to-side), AP (front-to-back), and TOP (top-to-top) as shown in Fig. 4.1. The anatomical human models TARO and HANAKO were considered to be standing in free space. Magnetic flux intensity was set to 0.1 mT and considered to be spatially uniform. By multiplying the ratio of the magnetic field strength of the reference level condition at each frequency to 0.1 mT, the results were converted into those for the reference level condition. The frequencies of the magnetic field were chosen to be 0.153 Hz, 20 Hz, 50 Hz, 167 Hz, 3350 Hz, 1 MHz, and 5 MHz which are relevant to the boundary values of reference level in the IEEE standard [11].

4.2.2. Computational Settings

The SPFD method described in Section 2.3.1 was applied to compute the induced electric field in the body. The stopping criteria of the Bi-CGSTAB iterative procedure was set at 10^{-8} measured by the relative residual norm of the equation solution.

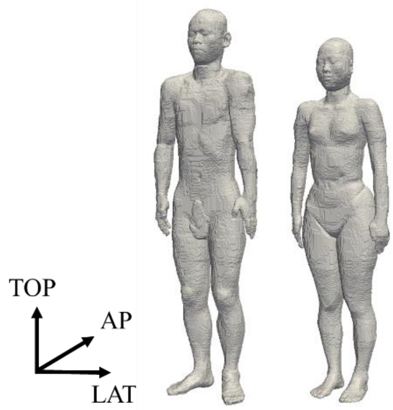

Figure 4.1 Anatomical human models along with exposure scenario.

4.3. Results

Figure 4.2 shows the distribution of the internal electric field in terms of AP direction exposure (results for 50 Hz and 1 MHz are shown as representative cases) in TARO and HANAKO. Figure 4.3 shows the distribution of the induced internal current density for the same conditions, models, and configurations as in Figure 4.2. In all the cases, both the electric field strength and current density are relatively high around the periphery of the torso, where the body cross section is the largest. On the contrary, they decrease around the ends of limbs where the cross sections are smaller. This is a common qualitative feature, regardless of the frequency or male/female differences.

Table 4.1 shows the 99th percentile values of induced internal electric fields for each body part ("Brain", "Heart", "Limbs", and "Other Tissues") as functions of frequency. Figure 4.4 was derived by converting the computational results in Table 4.1 into the reference level conditions for controlled environments in the IEEE standard by the method mentioned in section 4.2.1.

Together with these results, the analytical solutions for magnetic induction of the homogeneous elliptical cross-sectional model in IEEE standard [11]

$$E = 2\pi f B \frac{\sqrt{(a^2u)^2 + (b^2v)^2}}{a^2 + b^2} \tag{4.1}$$

are plotted, where f, B, a and b, u, and v are the frequency, magnetic flux density, semi-major and semi-minor diameter of the ellipse, and the electric field evaluation point in the ellipse, respectively. Note that a, b, u, and v adopt different values depending on the exposure scenario (e.g. sagittal or coronal direction exposure) in the IEEE standard [11]. The severest condition value (i.e. that for which the induced electric fields is largest) was chosen for each body part. The parameters applied to the homogeneous elliptical cross-sectional model for each body part are listed in Table 4.2.

Among the three different magnetic field orientation cases, maximum values are shown in the AP direction exposure case at the majority of frequencies for "Limbs" and "Other Tissues" in Table 4.1. In the same table, the induced electric fields exceeded that of the elliptical model in most cases of the brain and in the cases of AP exposure of the limbs and other tissues. As for Fig. 4.4, for "Brain", "Limbs", and "Other Tissues", the electric field intensities exceed the basic restriction in certain magnetic field orientations and frequency cases.

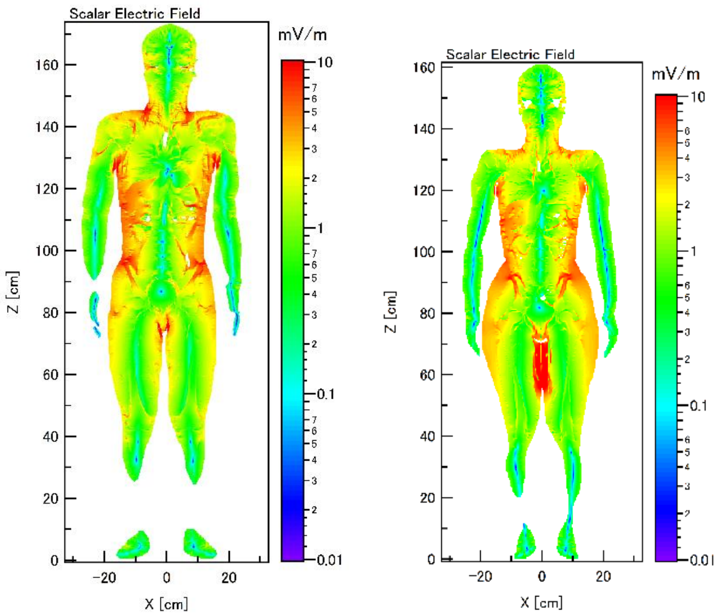

(a)

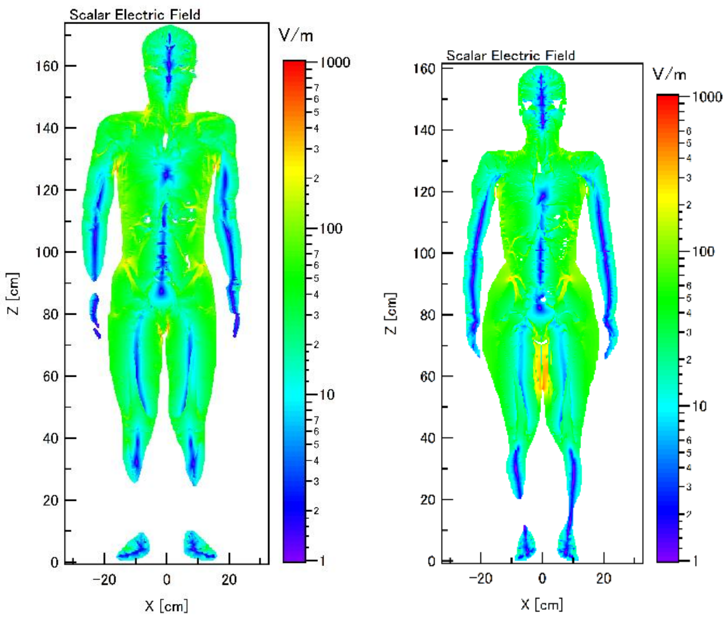

(b)

Figure 4.2 Distribution of the internal electric field induced by the time-varying uniform magnetic field (0.1 mT, (a) 50Hz, and (b) 1 MHz) for AP-direction exposure in a Japanese male (TARO) and female (HANAKO) model.

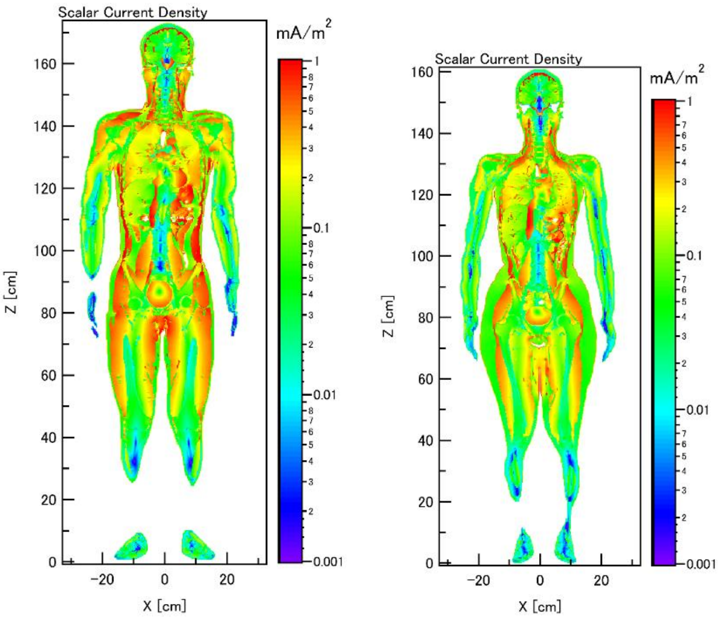

(a)

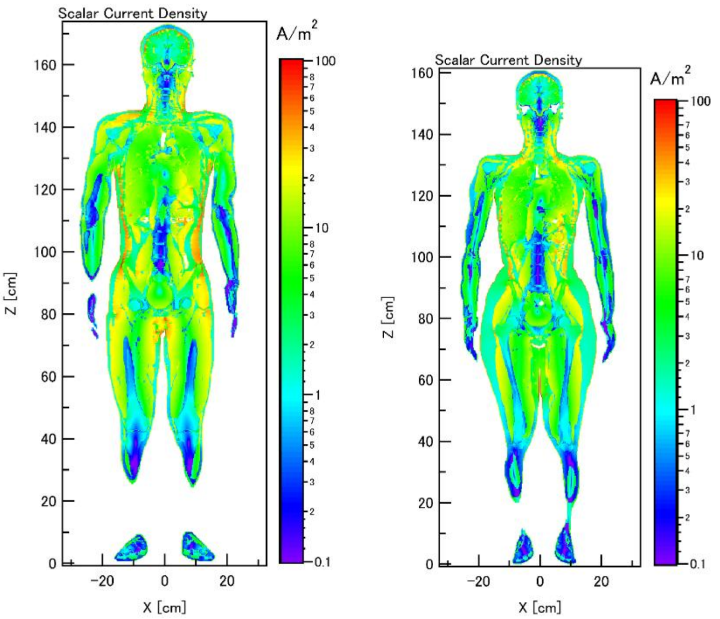

(b)

Figure 4.3 Distribution of the induced internal current density for same conditions, models and configurations as Fig. 4.2.

Table 4.1 Internal electric fields in body parts induced by uniform magnetic fields (0.1 mT).

		99th percentile values of induced internal electric field [mV/m]						Induced internal electric fields in IEEE elliptical cross-sectional model [mV/m]
		LAT		AP		TOP		
		TARO	HANAKO	TARO	HANAKO	TARO	HANAKO	
Brain	0.153 Hz	**1.12×10^{-2}**	**9.96×10^{-3}**	**9.75×10^{-3}**	**9.38×10^{-3}**	**8.46×10^{-3}**	**6.91×10^{-3}**	4.99×10^{-3}
	20 Hz	**1.30**	**1.16**	**1.16**	**1.11**	**1.00**	**0.840**	0.652
	50 Hz	**2.86**	**2.54**	**2.61**	**2.48**	**2.24**	**1.93**	1.63
	167 Hz	**9.31**	**8.19**	**8.43**	**8.01**	**7.20**	**6.26**	5.44
	3350 Hz	**182**	**161**	**165**	**157**	**140**	**123**	109
	1 MHz	**4.92×10^{4}**	**4.32×10^{4}**	**4.49×10^{4}**	**4.19×10^{4}**	**3.77×10^{4}**	**3.36×10^{4}**	3.26×10^{4}
	5 MHz	**2.30×10^{5}**	**2.01×10^{5}**	**2.11×10^{5}**	**1.95×10^{5}**	**1.77×10^{5}**	1.59×10^{5}	1.63×10^{5}
Heart	0.153 Hz	1.23×10^{-2}	1.25×10^{-2}	**1.31×10^{-2}**	8.90×10^{-3}	1.16×10^{-2}	9.90×10^{-3}	1.30×10^{-2}
	20 Hz	1.51	1.53	1.62	1.10	1.41	1.20	1.7
	50 Hz	3.37	3.41	3.59	2.46	3.03	2.60	4.25
	167 Hz	11.0	11.0	11.5	7.86	9.54	8.11	14.2
	3350 Hz	201	202	208	144	173	146	285
	1 MHz	4.50×10^{4}	4.53×10^{4}	4.71×10^{4}	3.75×10^{4}	3.89×10^{4}	3.23×10^{4}	8.50×10^{4}
	5 MHz	2.19×10^{5}	2.17×10^{5}	2.29×10^{5}	1.85×10^{5}	1.87×10^{5}	1.56×10^{5}	4.25×10^{5}
Limbs	0.153 Hz	7.50×10^{-3}	7.66×10^{-3}	**1.01×10^{-2}**	**2.57×10^{-2}**	6.42×10^{-3}	5.20×10^{-3}	8.27×10^{-3}
	20 Hz	0.962	0.992	**1.28**	**3.11**	0.813	0.662	1.08
	50 Hz	2.39	2.47	**3.17**	**7.39**	2.00	1.63	2.7
	167 Hz	8.14	8.33	**10.8**	**25.4**	6.81	5.56	9.03
	3350 Hz	164	166	**219**	**537**	138	113	181
	1 MHz	5.07×10^{4}	4.95×10^{4}	**7.11×10^{4}**	**1.80×10^{5}**	4.35×10^{4}	3.55×10^{4}	5.41×10^{4}
	5 MHz	2.55×10^{5}	2.48×10^{5}	**3.62×10^{5}**	**9.33×10^{5}**	2.19×10^{5}	1.79×10^{5}	2.70×10^{5}
Other Tissues	0.153 Hz	1.25×10^{-2}	9.58×10^{-3}	**2.17×10^{-2}**	**1.72×10^{-2}**	1.46×10^{-2}	1.09×10^{-2}	1.58×10^{-2}
	20 Hz	1.58	1.22	**2.73**	**2.18**	1.81	1.37	2.06
	50 Hz	3.87	3.01	**6.72**	**5.42**	4.40	3.35	5.16
	167 Hz	13.3	10.2	**23.4**	**18.7**	15.2	11.6	17.2
	3350 Hz	268	205	**476**	**382**	307	236	346
	1 MHz	8.26×10^{4}	6.30×10^{4}	**1.55×10^{5}**	**1.22×10^{5}**	1.00×10^{5}	7.68×10^{4}	1.03×10^{5}
	5 MHz	4.15×10^{5}	3.15×10^{5}	**7.82×10^{5}**	**6.08×10^{5}**	5.11×10^{5}	3.85×10^{5}	5.16×10^{5}

Table 4.2 Parameters Applied to Homogeneous Elliptical Cross-sectional Model.

Body Part	Parameters			
	a	*b*	*u*	*v*
Brain	10.5	9	9	0
Heart	90	17	14	18
Limbs	42	9	9	0
Other Tissues	90	17	17	0

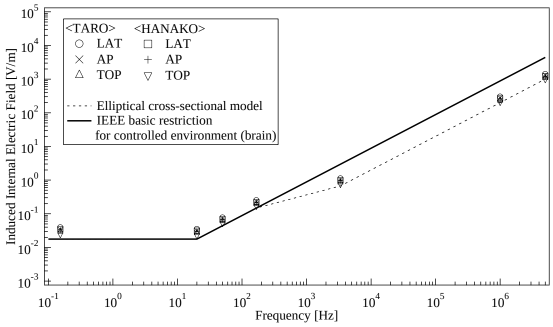

(a) Brain

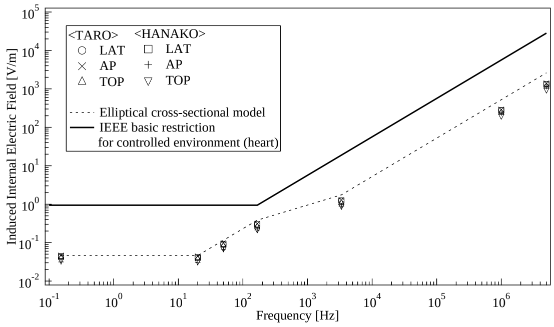

(b) Heart

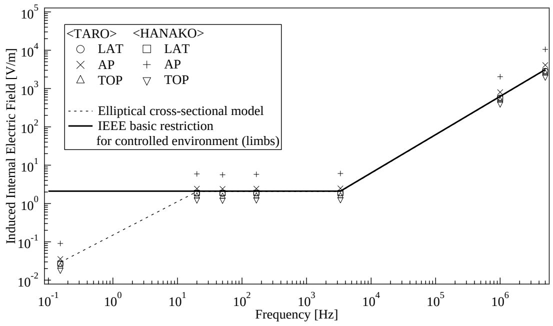

(c) Limbs

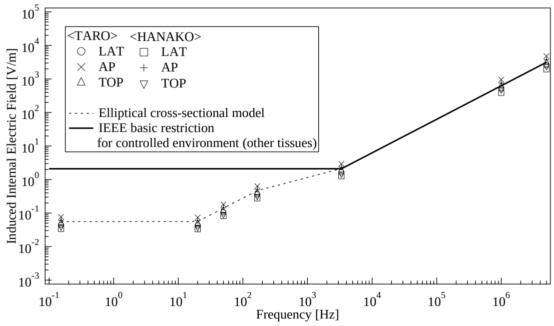

(d) Other Tissues

Figure 4.4 99th percentile values of induced electric fields in (a) Brain, (b) Heart, (c) Limbs and (d) Other tissues by uniform magnetic fields of the strength at reference levels in a controlled environment (IEEE standard) with Analytical solutions of the homogeneous elliptical models for magnetic induction.

As a factor in the exceedance of the basic restriction mentioned above, previous study [16] have pointed out the influence of the tissue surrounding the target body part. To examine the effect of injection currents from other organs, we considered an additional case of computation using the TARO model. In this case, the “Brain” is assumed to be isolated from the body in the free space (isolated exposure condition). The result is shown in Figure 4.5, along with the result of the whole-body exposure case (identical to Figure 4.2 (a)). Note that the contour of the whole brain in Figure 4.5 (a) corresponds to the projection of an entire brain, whereas the figure displays a single cross-section. As shown in the figure, the induced internal electric field intensity for the isolated exposure case is lower than that for the whole-body exposure case. Table 4.3 was derived by converting these results into the reference level conditions for controlled environments in the IEEE standard. In the isolated exposure condition, the induced electric field is lower than the values for both the whole-body exposure case and IEEE elliptical cross-sectional model (and thus, the basic restriction).

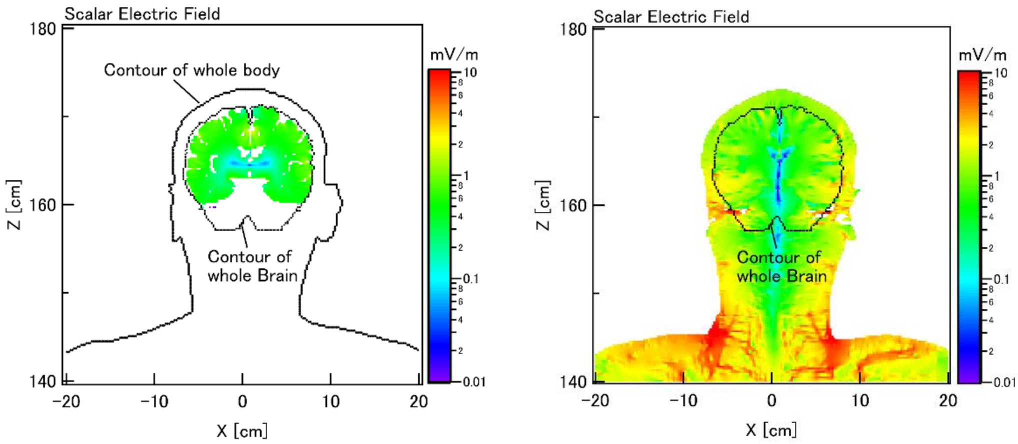

(a) (b)

Figure 4.5 Distribution of the internal electric field induced by the time-varying uniform magnetic field (0.1 mT, 50Hz, AP-direction) when (a) the “Brain” is isolated from the body, compared to (b) the whole-body exposure case.

Table 4.3 Comparison of internal electric field induced by the uniform magnetic field (50Hz, AP-direction) of exposure reference levels in a controlled environment (IEEE standard).

Case	99th percentile value of induced internal electric fields [mV/m]
Isolated exposure case (Brain)	33.9
Whole-body exposure case	70.7
IEEE elliptical cross-sectional model	44.2

4.4. Discussion

In Fig. 4.2 and 4.3, the electric field strength and current density tend to be higher in areas with larger cross-sectional areas as a common tendency. This may be attributed to Faraday's law, by which a larger eddy current occurs at the body part of a larger cross section. On the other hand, there is a significant difference between the results for TARO and HANAKO in that the electric field strength and the cureent density around the inner thighs of HANAKO are significantly higher than those of TARO. This is because the inner thighs are in contact with each other in the case of HANAKO, which produces a local circulating current, as discussed in a previous study by Aga *et al*. [16].

Among the three different magnetic field orientation cases, maximum values are shown in the AP direction exposure case at the majority of frequencies for "Limbs" and "Other Tissues" according to Table 4.1. It is assumed that the magnetic flux which passes through the exposed area (thus, also the induced electric field by the Faraday's law) tends to be larger in the AP direction for these body parts. The electric field strengths of TARO tend to be higher than those of HANAKO in most cases. This may be explained by the difference in their body sizes as described above, that is, TARO has a larger body size than HANAKO.

According to Figure 4.4, the analytical solutions of the elliptical cross-sectional model are in good qualitative agreement with the computed internal electric field, though not in quantitative agreement. For certain body parts, the computed internal electric fields exceed those of the elliptical cross-sectional model (most cases for "Brain", AP direction exposure cases for "Limbs" and "Other Tissues"). Consequently, for "Brain", "Limbs", and "Other Tissues", the electric field strengths exceed the basic restriction in certain magnetic field orientations and frequency cases.

On the other hand, electric field intensities are lower than the basic restriction for "Heart" in all cases. Such discrepancies between the results derived using the anatomical human model and those in elliptical cross-sectional model may result from the complex structure of the anatomical human models used. This has been suggested by several previous studies concerning dosimetry that employed anatomical human models. In the derivation of reference level in the IEEE standard, each body part is simulated using isolated homogeneous elliptical cross-sectional models, while the inner organs such as the brain or heart are surrounded by other organs and are subject to injection currents from other organs.

The above-mentioned influence from the surrounding tissue was confirmed by the validation shown in Fig. 4.5 and Table 4.3, in which the induced electric field for the isolated exposure condition is lower than that for the whole-body exposure case. This example may suggest that the effect of the injected current from the surrounding organs is considerable, that is, the injection current flow into/out of the brain from the surrounding organs increasing the maximum electric field strength in the case of the full model, whereas this phenomenon does not occur in the isolated case.

Additionally, the inhomogeneity of the electrical constants in the human body model and the effect of posture may affect the level difference between the human model and the homogeneous elliptical cross-sectional model. To clarify these concerns, further studies are needed.

4.5. Conclusion

In this chapter, the induced electric fields by uniform magnetic fields from ELF to intermediate frequencies in various body parts were determined and compared to the basic restriction in the IEEE C95.1$^{\text{TM}}$-2019 standard. Under the magnetic field exposure with strength of reference level, the computed induced electric fields exceeded the basic restriction for certain body parts and conditions. This may result from the discrepancy between the anatomical human model and the isolated elliptical cross-sectional model. Further studies are required in order to investigate the applicability of computational results using the anatomical human model to the derivation of reference levels.

Chapter 5
Dosimetry of Internal Electric Fields for Simultaneous Exposure to ELF Electric and Magnetic Fields With Phase Difference

5.1. Overview

This chapter investigated the impact of external electric and magnetic field phase differences on the induced electric field in anatomical human models. This was done under simultaneous exposure to a spatially uniform vertical electric field and horizontal magnetic fields at 50 Hz. Our computational findings revealed that the strength of the induced electric field fluctuates with the phase difference and that the variation caused by this difference varies across different body parts. The basic restrictions of the ICNIRP guidelines were met under the simultaneous exposure to electric and magnetic fields at the reference level, even when considering the phase difference.

The results presented here were published in [74].

5.2. Methods

5.2.1. Computation of Induced Electric Field by Electric and Magnetic Fields

The induced electric field within the human body is separately computed for electric and magnetic field exposures. These results are superimposed during post-processing to account for the phase difference between the electric and magnetic fields, simulating the induced electric field for simultaneous exposure.

The two-step method combining fast multipole surface charge and SPFD methods described in Chapter 3 was used to compute the induced electric field in humans for electric field exposure. The stopping criteria of the Bi-CGSTAB iterative procedure was set at 10^{-8} and 10^{-6} in the 1st and 2nd step of the method, respectively, in terms of the relative residual norm of the equation solution. The SPFD method described in Section 2.3.1 was used to compute the induced electric field in humans for magnetic field exposure. The stopping criteria of the Bi-CGSTAB iterative procedure was set at 10^{-6}.

5.2.2. Vector Addition of Induced Electric Fields by External Electric and Magnetic Fields

We assume a phase difference between the voltage and current of the power line and consider the relationship between the phase difference and the induced electric field. Focusing on the electromagnetic field surrounding the power line, the power line's voltage and current generate electric and magnetic field respectively (Fig. 5.1 (a)). A phase difference (–90° to +90° range) is known to occurs between the voltage V and the current I, depending on the power flow condition (power supply and demand), the impedance of the transmission and distribution lines, and the installation of phase modulating equipment [44], [45]. The lagging phase (–90° to 0° range) is introduced when the impedance or load is inductive, while the advancing phase (0° to +90° range) is introduced when the impedance or load is capacitive. If the phase delay of the current I with respect to the voltage V is θ, the following equation holds:

$$
\begin{aligned}
V &= V_0 e^{j\omega t} \\
I &= I_0 e^{j(\omega t - \theta)}
\end{aligned}
\tag{5.1}
$$

where V_0 and I_0 are the amplitudes of voltage and current, respectively. Since the external electric field $\boldsymbol{E}_{ext}$ and the external magnetic field $\boldsymbol{B}_{ext}$ are in phase with V and I, respectively, they are expressed as follows:

$$
\begin{aligned}
\boldsymbol{E}_{ext} &= \boldsymbol{E}_{ext}^{(0)} e^{j\omega t} \\
\boldsymbol{B}_{ext} &= \boldsymbol{B}_{ext}^{(0)} e^{j(\omega t - \theta)}
\end{aligned}
\tag{5.2}
$$

Here, $\boldsymbol{E}_{ext}^{(0)}$ and $\boldsymbol{B}_{ext}^{(0)}$ are the amplitudes of the external electric and magnetic fields, respectively. Based on Eqs. (5.1) and (5.2), and considering that the induced electric field due to the electric field is advanced by 90° compared to the external electric field because of capacitive current's nature and the induced electric field due to the magnetic field is delayed by 90° compared to the external magnetic field by Faraday's law, the induced electric field in the body due to the electric and magnetic field can be expressed as follows:

$$
\begin{aligned}
\boldsymbol{E}_{in}^{(\boldsymbol{E})} &= \boldsymbol{E}_{in}^{(\boldsymbol{E})(0)} e^{j(\omega t + 90°)} \\
\boldsymbol{E}_{in}^{(\boldsymbol{B})} &= \boldsymbol{E}_{in}^{(\boldsymbol{B})(0)} e^{j(\omega t - \theta - 90°)}
\end{aligned}
\tag{5.3}
$$

where $\boldsymbol{E}_{in}^{(\boldsymbol{E})(0)}$ and $\boldsymbol{E}_{in}^{(\boldsymbol{B})(0)}$ are the amplitudes of the induced electric and magnetic fields in the body, respectively. In other words, the electric field, induced by the magnetic field, lags behind by 180° + θ. The vector diagram of the induced electric field components in the body caused by the electric and magnetic fields, as well as the external electromagnetic field, power line voltage and current, is shown in Fig. 5.1 (b).

If the current phase of the power line lags behind the voltage phase by θ, the same magnitude of phase difference also occurs between the induced electric field components due to magnetic and electric field exposures. Considering the phase difference, $\boldsymbol{E}_{in}^{(\boldsymbol{E})}$ and $\boldsymbol{E}_{in}^{(\boldsymbol{B})}$ denote the induced field due to exposure to electric and magnetic fields computed under the assumption that the external electric and magnetic fields were in phase. Then they are added, considering the phase factor $e^{-j\theta}$ to derive the induced electric field for simultaneous exposure to electromagnetic fields.

$$\boldsymbol{E}_{tot} = \boldsymbol{E}_{in}^{(\boldsymbol{E})} + \boldsymbol{E}_{in}^{(\boldsymbol{B})} e^{-j\theta} \tag{5.4}$$

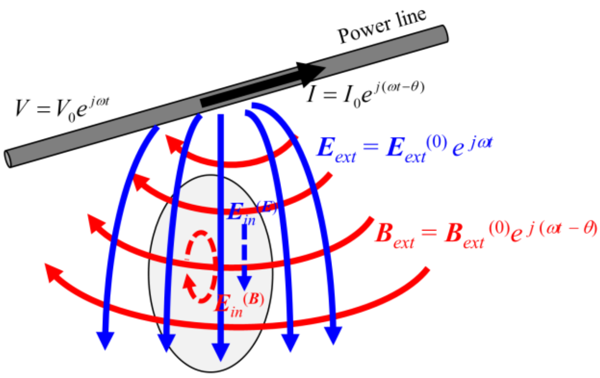

(a)

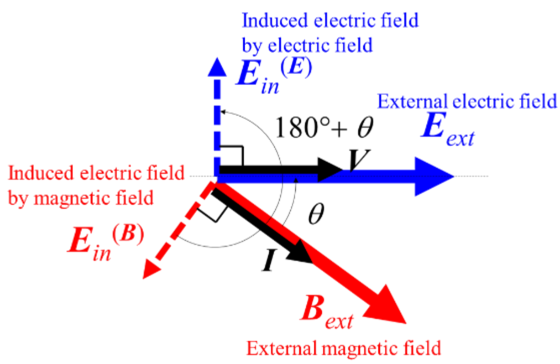

(b)

Figure 5.1 Representation of the relationship between the phase difference of voltage/current and the phase difference for electric/magnetic fields. (a) Relationship between line voltage/current and (b) vector diagram and electromagnetic fields.

5.3. Exposure Scenarios

We considered a scenario where a human is positioned beneath transmission lines. This would expose the human body model to a uniform vertical electric field and horizontal magnetic field. The impact of external field inhomogeneity on the induced electric field is detailed in [24]. Compared to the vertical component, the horizontal component of the electric field is negligible due to its weaker coupling with the human body. The frequency was 50 Hz. As shown in Fig. 5.2, the vertical electric field (E_z), left-right magnetic field (B_x), and front-back magnetic field (B_y) were considered. We examined two combinations of electric and magnetic fields for simultaneous exposure conditions: E_z and B_x and E_z and B_y, hereafter referred to as cases $E_z + B_x$ and $E_z + B_y$, respectively. Single electric or magnetic field exposures (E_z, B_x, and B_y) were also considered as reference cases. The scenarios described above are the most likely situations, but not necessarily the most extreme conditions (e.g., [26]). For example, maintenance workers of live electrical systems can assume different positions during their work, or a generic person can be lying on the ground for any reason. In addition, due to Faraday's law, the induced field strength in magnetic field exposure strongly depends on the area of the magnetic field crossing the body part. More specifically, it strongly depends on the size and posture of the human body. Note that in the ICNIRP RF guideilnes, extremely cases are not considered.

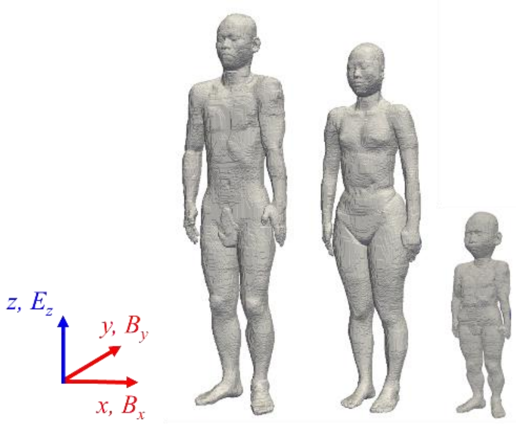

Figure 5.2 Alignment of the electric and magnetic field.

Initially, this study evaluated the fundamental characteristics of the induced electric field considering simultaneous exposure to electromagnetic fields and the phase difference between the electric and magnetic fields. Subsequently, we assessed the compliance of the induced electric field with the basic restrictions in the ICNIRP and IEEE standards.

The external field strength of the electric and magnetic field was aligned with the reference levels of the ICNIRP guidelines [9] and the IEEE C95.1™-2019 [3] at 50 Hz. The basic restrictions and reference levels of ICNIRP and IEEE are outlined in Tables 5.1 and 5.2, respectively. According to the ICNIRP guidelines, E_z = 5 kV/m and B_x = B_y = 0.2 mT for the general public, and E_z = 20 kV/m and B_x = B_y = 1 mT for occupational exposure, were assumed, respectively. Note that assuming the electromagnetic field strength equivalent to the reference level for occupational exposure may not be a realistic condition for the child model. In the IEEE standard, the reference level is E_z = 5 kV/m, B_x = B_y = 904 μT (head and torso), and 75.8 mT (limbs) under general public conditions.

Table 5.1 Basic restriction and reference level, as stipulated by ICNIRP guideline at 50 Hz.

	Basic restriction [mV/m]		Reference level	
	CNS of the head	Whole body	Electric field [kV/m]	Magnetic field [μT]
General public exposure	20	400	5	200
Occupational exposure	100	800	20	1000

Table 5.2 (a) Basic restriction and (b) reference level of IEEE C95.1™-2019 at 50 Hz

(a)

	Basic restriction [mV/m]			
	Brain	Heart	Limbs	Others
General public condition	14.725	943	2100	701
Controlled environment condition	44.25	943	2100	2100

(b)

	Reference level		
	Electric field [kV/m]	Magnetic field [μT] (head and torso)	Magnetic field [μT] (Limbs)
General public condition	5	904	75800
Controlled environment condition	20	2710	75800

5.4. Results

5.4.1. Fundamental Characteristics of Induced Electric Fields under Simultaneous Electromagnetic Field Exposure

To evaluate the impact of superposition and phase difference of external electromagnetic fields on induced electric field strength, the induced electric field in the body was computed for the simultaneous electromagnetic field exposure cases: (i) $E_z + B_x$ and (ii) $E_z + B_y$ (E_z = 20 kV/m and $B_x = B_y$ = 1 mT).

Fig. 5.3 illustrates the layer-averaged induced electric field on the horizontal cross-section in the male model. For the single exposure to E_z only, the induced field strength peaks at the neck (around z =150 cm), arms (around z = 90–120 cm), knees (around z = 40 cm), and ankles (around z = 0–10 cm) with a small cross-sectional area, thereby resulting in a small capacitive current. Conversely, exposure to only B_x or B_y induces higher field strength in the head (z =150–170 cm) and torso (z = 80–140 cm), where the large magnetic flux crossing the model leads to large eddy currents.

In the case of simultaneous exposure to external electric and magnetic fields, the induced electric field strength varies for different phase differences θ at 0°, 45°, and 90°.
The induced electric field for simultaneous exposure exceeds that of exposure to a single component of a magnetic or electric field, suggesting a constructive interference effect for most body parts. However, the effect is destructive at certain locations for the $E_z + B_x$ case (z = 60–80 cm and z = 90–100 cm).

Table 5.3 and Fig. 5.4 display the 99th percentile values of the induced electric fields in the brain, heart, and whole body in cases $E_z + B_x$ and $E_z + B_y$ when the phase difference between the electric and magnetic fields ranges from −90° to 90°. Table 5.3 shows the 99th percentile values of induced electric fields on the brain, heart, and whole body assuming simultaneous exposure with phase difference surpass those for separate electric or magnetic exposures. Specifically, in the heart, the electric fields for the cases of $E_z + B_x$ (83.4–63.0 [mV/m]) were 12% to 143%

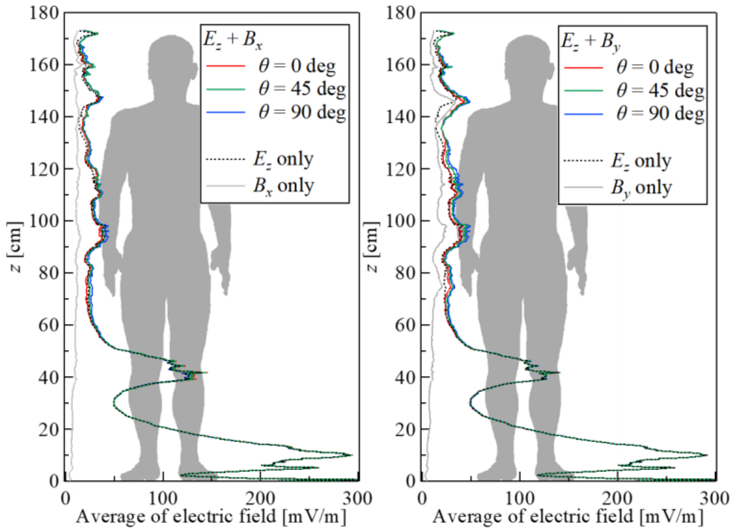

(a) (b)

Figure 5.3 Vertical distribution of induced electric field strength averaged in each horizontal cross section at z for simultaneous exposure. (a) $E_z + B_x$ and (b) $E_z + B_y$ (E_z = 20 kV/m and B_x = B_y = 1 mT) for the male model.

Table 5.3 99th %ile Values for induced electric fields in various body parts during simultaneous exposure of $E_z + B_x$ and $E_z + B_y$ (E_z = 20 kV/m, B_x = B_y = 1 MT) compared to single component exposure to E_z, B_x, and B_y only.

Model	Body part	99th percentile value of induced electric field [mV/m]								
		Single component exposure to electric / magnetic fields			Simultaneous exposure ($E_z + B_x$)			Simultaneous exposure ($E_z + B_y$)		
		E_z= 20kV/m	B_x= 1mT	B_y= 1mT	θ = 0°	θ =45°	θ =90°	θ = 0°	θ=45°	θ=90°
Male	Brain	37.4	29.8	27.7	34.3	33.1 (-3 %)	40.1 (17 %)	46.0	42.9 (-7 %)	37.5 (-18 %)
	Heart	56.4	34.3	36.0	83.4	78.0 (-6 %)	63.0 (-24 %)	86.0	80.1 (-7%)	63.4 (-26%)
	Whole Body	351.7	47.6	79.4	355.2	354.4 (-0.2%)	351.9 (-0.9%)	353.1	352.7 (-0.1%)	351.8 (-0.4%)
Female	Brain	36.5	26.8	25.8	41.0	39.8 (-3%)	38.0 (-7%)	45.5	42.3 (-7%)	36.9 (-19%)
	Heart	62.4	33.0	25.4	91.2	85.0 (-7%)	68.1 (-25%)	81.7	76.9 (-6%)	65.0 (-20%)
	Whole Body	550.6	37.7	69.3	552.0	551.7 (-0.1%)	550.7 (-0.2%)	550.4	550.5 (0.0%)	550.7 (0.1%)
Child	Brain	42.7	21.7	20.5	44.1	43.7 (-1%)	42.7 (-3%)	42.3	42.4 (0.2%)	42.7 (1%)
	Heart	39.3	20.6	17.8	53.3	50.1 (-6%)	41.7 (-22%)	53.6	50.4 (-6%)	41.9 (-22%)
	Whole Body	329.4	36.8	46.9	330.1	330.0 (-0.0%)	329.4 (-0.2%)	332.7	331.3 (-0.4%)	329.5 (-1%)

* The % Value in parentheses () represents the rate of change with respect to 0°.

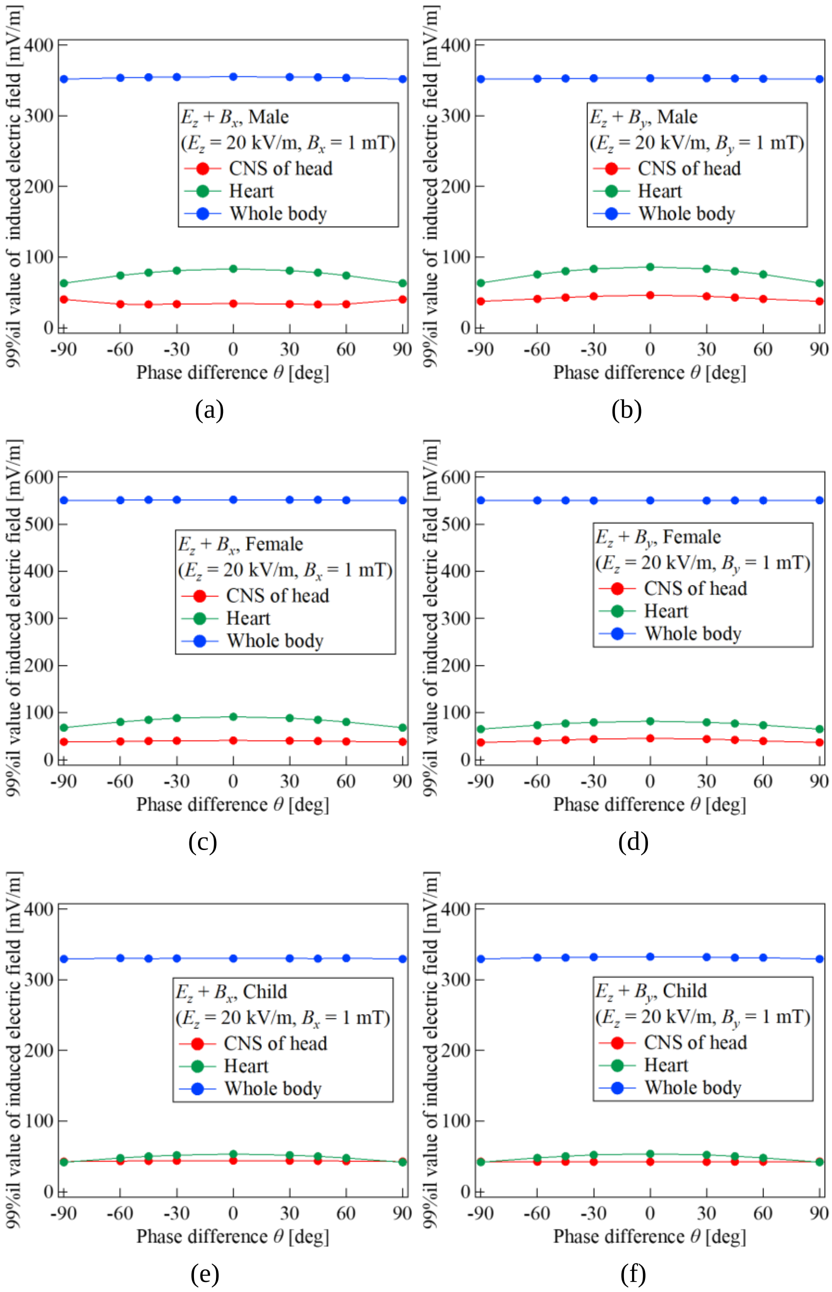

Figure 5.4 Phase difference dependence of induced electric field strength for each part for simultaneous exposure cases of (a) $E_z + B_x$ and (b) $E_z + B_y$ (where E_z = 20 kV/m, $B_x = B_y$ = 1 mT). Panels (a) and (b) depict the adult male model results; panels (c) and (d) depict the adult female model results; panels (e) and (f) depict results for the child model.

larger than those for the single electric field exposure case of E_z (56.4 mV/m) and B_x (34.3 [mV/m]) through θ = 0° to 90° for the male model. The exceptions were the conditions θ = 0° and 45° of the case $E_z + B_x$ for the male model, wherein the induced electric field strength was smaller than E_z only. The increase in simultaneous exposure relative to the single electric field exposure ranged from 6% to 48%. Note that although Fig. 5.4 shows only the calculated values at θ = 0°, ±30°, ±45°, ±60°, and ±90°, it has been confirmed that the synthesized induced electric field in the body varies sinusoidally with θ according to eq. (5.4) and that no peculiar peaks, etc., are generated at the thinned-out calculation points.

As demonstrated in Fig. 5.4, the induced electric field strength changes due to the phase change are symmetric around θ = 0°. Additionally, the effect of phase difference on induced electric field strength varies across exposure scenarios and body parts. The electric field in the heart decreases with phase difference, whereas that of the brain slightly increases in the case of $E_z + B_x$. Variation widths in the brain for all models concerning θ = 0° were 3%–17% for the $E_z + B_x$ case and 1%–18% for the $E_z + B_y$ case, both of which were smaller than those in the heart (i.e., 22%–25% for the $E_z + B_x$ case and 20%–26% for the $E_z + B_y$, as listed in Table IV). For both $E_z + B_x$ and $E_z + B_y$ exposure, the variation of the induced electric field with phase difference for the whole body is marginal because the maximum induced electric fields inside the whole body are observed around the ankle, where the induced electric field by electric induction dominates.

The variations in the phase difference between the external electric and magnetic fields induced changes in the electric field strength inside the body, which fluctuated for different body parts. Fig. 5.5 further clarifies this by illustrating a vector diagram of the induced electric field in the male model's body for the case $E_z + B_x$. The vector plot in the figure shows the value of each component of the induced electric field by the electric and magnetic field at the maximum phase of electric induction. The color map represents the effective value at single, 50 Hz cycle.

With a phase difference of 0°, the induced electric field strength at the front of the body is high but modest at phase differences of 45° and 90°. At a phase difference of 0°, the induced electric field components due to magnetic field induction at the front of the body align in the same direction as those due to electric field induction, resulting in constructive interference.

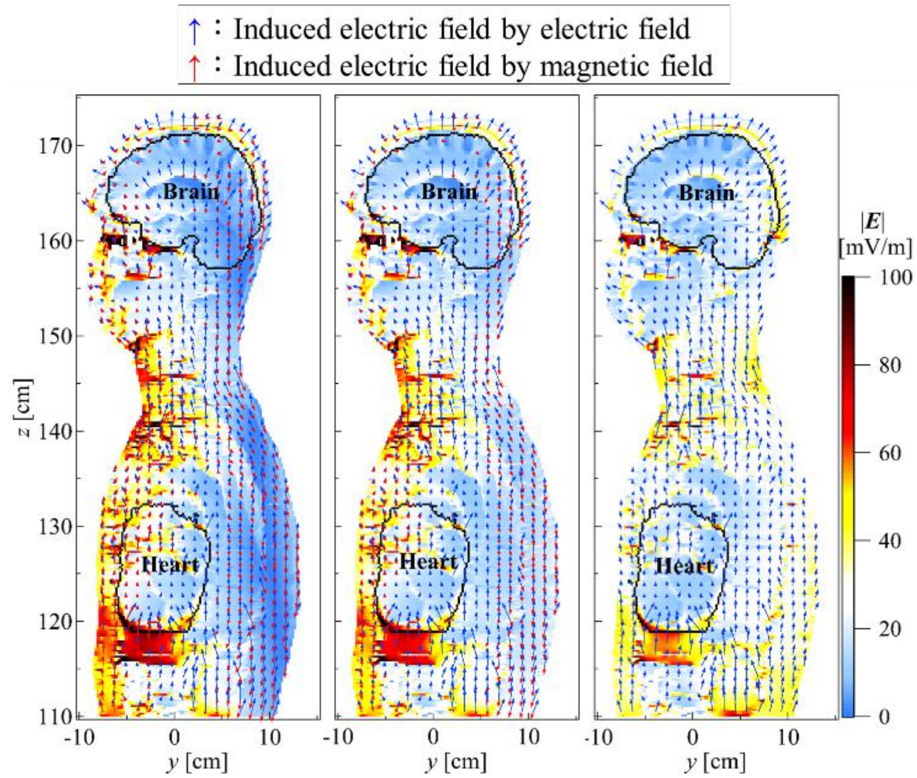

(a) (b) (c)

Figure 5.5 Induced electric field strength distribution in the male model for case of E_z + B_x (E_z = 20 kV/m, Bx = 1 mT) together with vector components for induction by single external electric and magnetic field with phase differences of (a) 0°, (b) 45°, and (c) 90°.

Conversely, the opposite tendency is observed at the back of the body, where the electric field directions induced by the external magnetic and electric fields are in opposition. The induced electric field components due to magnetic field induction at a phase difference of 45° are smaller than those at 0° and null at 90°. The total induced electric field strength at the front of the body subsequently increases while decreasing at the back of the body as the phase difference augments from 0° to 90°. Consequently, as shown in Fig. 5.4 (a), the heart's total induced electric field strength monotonically decreases.

The brain's total induced electric field strength exhibits a complex phase difference dependency because the induced electric field component induced by external electric and magnetic fields strengthen each other at the front of the head but weaken each other at the back of the head.

5.4.2. Compliance Evaluation with the Basic Restriction Under Simultaneous Electromagnetic Field Exposure Conditions at the ICNIRP and IEEE Reference Levels

We assessed compliance with basic restrictions (DRLs) under simultaneous exposure to electromagnetic fields at the reference level of international guidelines such as ICNIRP guidelines [9] and the IEEE C95.1^{TM}-2019 [11]. Given the symmetry in induced electric field strength variations concerning $\theta = 0°$ from Section 5.4.1, we only considered $\theta > 0°$ in this analysis.

Table 5.4 presents the induced electric fields computed under simultaneous exposure of the $E_z + B_x$ and $E_z + B_y$ scenarios. We assumed electromagnetic field strengths equivalent to the public and occupational exposure reference levels established in the ICNIRP guidelines. As indicated in Table 5.4, the induced electric fields for public and occupational exposure scenarios, as well as for all phase differences, remained significantly below the basic restrictions of 20 mV/m (CNS of the head) and 400 mV/m (all tissues of the head and body) for general public exposure. The respective values for occupational exposure were 100 mV/m (CNS of the head) and 800 mV/m (all tissues of the head and body), as detailed in Table 5.1. The induced electric field strength variation due to phase changes ranged from −19% to +15% for the CNS of the head and from −0.9% to 0% for the whole body across all models, as shown in Table 5.4.

Table 5.5 displays the induced electric field calculated under simultaneous electromagnetic field exposure for the reference level conditions specified in IEEE C95.1^{TM}-2019. As the reference levels and basic restrictions under controlled environment conditions are proportional to those under general public conditions, we only evaluated conformity under general public conditions. Cases where the induced electric field exceeded the basic restriction listed in Table 5.2, are highlighted in bold in Table 5.5. For scenarios $E_z + B_x$ and $E_z + B_y$ for all models, the induced electric fields in the brain exceeded the basic restriction. The same applied to the limbs in the $E_z + B_x$ scenario for the female model and in all phases of the $E_z + B_y$ scenario for all models. The variation widths of induced electric field strength due to phase changes for the $E_z + B_x$ cases ranged from −2% to +20% for the brain, −25% to −3% for the heart, −0.2% to +0.3% for the limbs, and −16% to −2% for others, respectively, across all models. Those for the $E_z + B_y$ cases were −6% to −1% for the brain, −27% to −3% for the heart, −0.1% to +0.2% for the limbs, and −11% to −1% for others, respectively.

Table 5.4 Phase difference dependence of induced electric field strength for CNS head and whole body under simultaneous exposure case $E_z + B_x$ and $E_z + B_y$ of ICNIRP reference level for (a) general public and (b) occupational exposure at 50 Hz.

(a)

Model	Phase difference θ	99th percentile value of induced electric field [mV/m] assuming general public exposure (E_z = 5 kV/m, $B_x = B_y$ = 0.2 mT) $E_z + B_x$				$E_z + B_y$			
		CNS of the head	Rate of change	Whole body	Rate of change	CNS of the head	Rate of change	Whole body	Rate of change
Male	0°	8.1	—	63.1	0.0%	10.5	0%	63.1	0.0%
	30°	7.9	-1%	63.1	0.0%	10.2	-3%	63.0	0.0%
	60°	7.9	-2%	63.0	-0.1%	9.4	-10%	63.0	-0.1%
	90°	9.2	15%	63.0	-0.2%	8.8	-16%	63.0	-0.1%
Female	0°	10.0	0.0%	138.0	0.0%	10.4	0%	137.6	0.0%
	30°	9.9	-1.1%	137.9	0.0%	10.1	-3%	137.6	0.0%
	60°	9.6	-4.1%	137.7	-0.2%	9.3	-10%	137.6	0.0%
	90°	9.2	-8.5%	137.7	-0.2%	9.1	-12%	137.7	0.0%
Child	0°	11.0	0.0%	82.5	0.0%	10.6	0.0%	82.9	0.0%
	30°	10.9	-0.3%	82.5	0.0%	10.6	0.1%	82.8	-0.2%
	60°	10.8	-1.3%	82.6	0.1%	10.6	0.4%	82.8	-0.2%
	90°	10.7	-2.5%	82.3	-0.2%	10.7	0.7%	82.4	-0.7%

(b)

Model	Phase difference θ	99th percentile value of induced electric field [mV/m] assuming occupational exposure (E_z = 20 kV/m, $B_x = B_y$ = 1 mT) $E_z + B_x$				$E_z + B_y$			
		CNS of the head	Rate of change	Whole body	Rate of change	CNS of the head	Rate of change	Whole body	Rate of change
Male	0°	34.3	0%	355.2	0.0%	46.0	0.0%	353.1	0.0%
	30°	33.6	-2%	354.8	-0.1%	44.6	-3.0%	353.0	0.0%
	60°	33.3	-3%	353.6	-0.5%	40.8	-11.3%	352.4	-0.2%
	90°	40.1	17%	351.9	-0.9%	37.5	-18.5%	351.8	-0.4%
Female	0°	41.0	0.0%	552.0	0.0%	45.5	0%	550.4	0.0%
	30°	40.5	-1.3%	551.9	0.0%	44.0	-3%	550.3	0.0%
	60°	39.0	-5.0%	551.0	-0.2%	40.0	-12%	550.5	0.0%
	90°	38.0	-7.3%	550.7	-0.2%	36.9	-19%	550.7	0.1%
Child	0°	44.1	0.0%	330.1	0.0%	42.3	0.0%	332.7	0.0%
	30°	43.9	-0.4%	330.3	0.0%	42.4	0.1%	332.1	-0.2%
	60°	43.4	-1.5%	330.6	0.2%	42.5	0.4%	331.2	-0.4%
	90°	42.7	-3.1%	329.4	-0.2%	42.7	0.9%	329.5	-1.0%

***** The "rate of change" represents the rate of change relative to the 0° phase difference value.

Table 5.5 Phase difference dependence of induced inner electric field strength for each body part under simultaneous exposure case (a) $E_z + B_x$ and (b) $E_z + B_y$ of ERL for general public condition in IEEE C95.1™-2019 at 50 Hz.

(a)

Model	Phase difference θ	99th percentile value of induced electric field [mV/m] assuming $E_z + B_x$ of general public condition ; E_z = 5 kV/m, B_x = 904 μT (head and torso), 75.8 mT (limbs)							
		Brain	Rate of change	Heart	Rate of change	Limbs	Rate of change	Others	Rate of change
Male	0°	**23.1**	0%	42.3	0%	2014	0.0%	55.8	0%
	30°	**23.6**	2%	41.2	-3%	2013	0.0%	54.5	-2%
	60°	**25.2**	9%	37.8	-11%	2012	-0.1%	51.7	-7%
	90°	**27.7**	20%	32.9	-22%	2010	-0.2%	52.1	-7%
Female	0°	**24.7**	0%	44.1	0%	**2144**	0.0%	51.5	0%
	30°	**24.5**	-1%	42.8	-3%	**2145**	0.0%	50	-3%
	60°	**24.3**	-2%	38.9	-12%	**2147**	0.1%	46.1	-10%
	90°	**24.9**	1%	33.1	-25%	**2151**	0.3%	43.1	-16%
Child	0°	**18.1**	0%	26.1	0%	1419	0.0%	42.6	0%
	30°	**18.2**	1%	25.4	-3%	1419	0.0%	41.7	-2%
	60°	**18.8**	4%	23.3	-11%	1421	0.1%	39.6	-7%
	90°	**20.1**	11%	20.1	-23%	1423	0.3%	38.3	-10%

(b)

Model	Phase difference θ	99th percentile value of induced electric field [mV/m] assuming $E_z + B_y$ of general public condition ; E_z = 5 kV/m, B_y = 904 μT (head and torso), 75.8 mT (limbs)							
		Brain	Rate of change	Heart	Rate of change	Limbs	Rate of change	Others	rate of change
Male	0°	**27.4**	0%	44	0%	**3244.9**	0.0%	84.7	0%
	30°	**26.9**	-2%	42.8	-3%	**3244.8**	0.0%	83.9	-1%
	60°	**26.2**	-4%	39.5	-10%	**3244.4**	0.0%	83.3	-2%
	90°	**25.7**	-6%	34.5	-22%	**3242.9**	-0.1%	83.5	-1%
Female	0°	**25.9**	0%	36.1	0%	**7264.1**	0.0%	78.4	0%
	30°	**25.5**	-2%	34.9	-3%	**7264.3**	0.0%	76.8	-2%
	60°	**24.5**	-5%	31.7	-12%	**7264.8**	0.0%	73.1	-7%
	90°	**24**	-7%	26.5	-27%	**7264.7**	0.0%	70.7	-10%
Child	0°	**20.3**	0%	24.1	0%	**3976.1**	0.0%	51.5	0%
	30°	**20**	-1%	23.4	-3%	**3976.8**	0.0%	50.4	-2%
	60°	**19.2**	-5%	21.2	-12%	**3979.2**	0.1%	47.9	-7%
	90°	**19**	-6%	17.9	-26%	**3982.2**	0.2%	46	-11%

*1: The "rate of change" represents the rate of change relative to the 0° phase difference value.

*2: Cases where the induced electric field exceeded the basic restriction are marked in Bold.

5.5. Discussion

This chapter investigated the impact of phase differences on induced electric fields under simultaneous exposure to uniform electric and magnetic fields at reference levels, as outlined by various international guidelines and standards. Our computational findings revealed that induced electric field strength varies with a phase difference, with the degree of variation differing across body parts. Specifically, we observed a decrease in the electric field within the heart as phase difference increased, while the variation within the brain was comparatively smaller. We also examined the compliance with the basic restrictions in exposure guidelines, accounting for phase differences under simultaneous exposure at reference levels. While we were able to confirm conformity under ICNIRP guidelines, there were some isolated instances of basic restriction exceedance according to the IEEE standard.

The phase difference-related variations in induced electric field strengths can be attributed to changes in phase angle between induced electric fields prompted by external electric and magnetic fields. As Fig. 5.1 (b) elucidates, as the phase difference between external electric and magnetic fields increases, the component of induced electric fields $\boldsymbol{E}_{in}^{(\boldsymbol{B})}$ parallel to $\boldsymbol{E}_{in}^{(\boldsymbol{E})}$ decreases. If $\boldsymbol{E}_{in}^{(\boldsymbol{B})}$ and $\boldsymbol{E}_{in}^{(\boldsymbol{E})}$ constructively interfere (i.e., they are in similar directions) at a phase difference of 0°, the total induced electric field strength will decrease with an increasing phase difference. Conversely, the total induced electric field strength increased with the phase difference if they interfere destructively. This perspective effectively explained the observed negative dependency of induced electric field strength on phase difference in the heart, as illustrated in Fig. 5.4.

The varying phase difference dependency of induced electric field strength among different body parts could be explained by the body part's relative location to the center of the eddy current. In the brain, located near the center of the local eddy current in the head, the variation width was relatively small ($E_z + B_x$: 17%, $E_z + B_y$ 18%, for the male model, as presented in Table 5.3). Here, $\boldsymbol{E}_{in}^{(\boldsymbol{B})}$ and $\boldsymbol{E}_{in}^{(\boldsymbol{E})}$ interfere *both* constructively and destructively. However, the heart, situated outside the center of the local eddy current in the torso, exhibited a larger variation width than the brain ($E_z + B_x$: 25%, $E_z + B_y$: 26% for the male model). This is because $\boldsymbol{E}_{in}^{(\boldsymbol{B})}$ and $\boldsymbol{E}_{in}^{(\boldsymbol{E})}$ only interfere constructively or destructively in the heart, as shown in Fig. 5.5.

Table 5.3 also showed that the heart most prominently demonstrates the effects of superimposed electric and magnetic fields and phase differences. The increase in induced electric field in simultaneous exposure relative to single electric field exposure ranged from 31% to 52% for the heart, 0%–25% for the brain, and 0%–1% for the whole body across all models. The brain and the whole body were less sensitive to phase difference than the heart since these body parts are dominated by the induced electric field due to single electric field exposure. For the whole body, only single electric field exposure should be considered to derive the maximum value of the induced electric field, as it was minimally dependent on the phase difference.

We also explored conformity with international guidelines and standards. As noted in Sec. 5.4.2, the basic restriction of the ICNIRP guideline is met even when considering simultaneous exposure to external electric and magnetic fields at the guideline's reference level and their phase difference for all models. This may be due to the fact that the head and whole body are less sensitive to phase differences, as previously discussed. The ratio of the induced electric fields to the basic restriction ranged from 16 to 69% in Table 5.4. This ratio takes the minimum in the case of $E_z + B_x$ with the general public exposure level for the male model, $\theta = 90°$ at the whole body and takes the maximum in the case of $E_z + B_x$ with occupational exposure level for the female model, $\theta = 0°$ at the whole body. Importantly, a past study [42] considering simultaneous exposure under in-phase conditions (American male, magnetic field 100μT + electric field 5 kV/m) also reported results below the basic restriction of the ICNIRP guideline, albeit in an earlier version of the guideline [70]. While a direct comparison cannot be made due to their reliance on a previous guideline version, our findings corroborated that the ICNIRP basic restriction is still met even when considering the effect of phase difference.

Conversely, the induced electric field for the reference level strength of IEEE standard exceeded the basic restriction. Past research [16] and chapter 4 suggested that the induced electric field may surpass the basic restriction even under separate exposures to magnetic fields at reference level strength. The basic restriction exceedance was most apparent in the limbs for the female model across all models, potentially due to the inner sides of the female model being in contact with each other, as suggested in [16]. As discussed in [71], skin-to-skin contact does not result in nerve stimulation, which aligns with the IEEE standard. Of all subject parts considered for basic restrictions, the heart was the most sensitive to the phase difference, even though the induced electric fields in the heart remained below the basic restriction for all cases.

5.6. Conclusion

This chapter computed the induced electric field under simultaneous exposure to spatially uniform ELF electric and magnetic fields considering the phase difference of them. The results demonstrated that induced electric field strength varied with phase difference and that this variation differs across body parts. The width of this variation depends on the relative location of the subject body part, which can be characterized by the eddy current. Of all the body parts, the heart demonstrated the most pronounced effect of superimposing electric and magnetic fields and phase differences. Despite considering the effect of phase difference, the basic restriction of ICNIRP guideline is still satisfied under the simultaneous exposure of electric and magnetic fields with reference level. Even under these conditions, the induced electric field strength was at most 69% of the basic restriction of the ICNIRP guideline.

Chapter 6
Summary

The adverse health effects of electromagnetic fields have long been of great concern, in particular, in the vicinity of electric power facilities installed adjacent to the living areas of the general public. Hence it is important to consider the safety of human health from electromagnetic fields generated around these facilities. The frequencies of environmental electromagnetic fields generated around power facilities range from commercial frequencies to intermediate frequencies. The dominant effect of electromagnetic fields from ELF to intermediate frequencies on the human body is stimulation of nerves by induced currents at frequencies below 100 kHz. International guidelines such as ICNIRP guidelines or IEEE standard offer protection from environmental electromagnetic fields.

In the international guidelines mentioned above, a basic restriction, which is the permissible value of the electric field induced in the human body by electromagnetic fields (induced electric field), and a limit value for the strength of external electromagnetic fields (reference level) below the basic restriction are specified. Regarding the validity of these reference level, we found the following issues 1) and 2).

1) Reference level validity in IEEE standards: The reference level for magnetic fields in the IEEE standard is based on the analytical solution of the induced electric field in a homogeneous ellipsoid model in a uniform magnetic field, and it is difficult to say that the coupling between magnetic fields and the human body is considered more precisely than the reference level in the ICNIRP guidelines, which is based on the results of electromagnetic field analysis using anatomical human body models.
2) Reference level margins under conditions of simultaneous exposure to electromagnetic

fields: The reference levels in the international guidelines are defined for separate exposure to electric and magnetic fields, but since exposure to both electric and magnetic fields can occur around real electric power facilities, it is necessary to verify whether the reference levels are marginally safe as threshold values under such conditions. In addition, a phase difference occurs between electric and magnetic fields around some power facilities, but the effect of this phase difference on induced electric fields in the body under conditions of simultaneous exposure to electromagnetic fields has not been clarified.

In relation to issues 1) and 2), another practical issue in using dosimetry concerning electric field is addressed:

3) Necessity for Advancement of dosimetry methods for electric fields: The computational cost of conventional dosimetry methods of electric fields is enormous. There is no efficient dosimetry method, and there are few examples of electric field dosimetry calculations.

The purpose of this study is to verify the validity of the reference levels for electromagnetic fields at low to intermediate frequencies in the international guidelines, as described in 1) and 2) above, based on dosimetry using an anatomical human body model. In solving issues 1) and 2), we have enhanced the dosimetry method of electric fields at low frequencies in response to issue 3).

First, we developed a two-step electromagnetic field analysis method based on the fast multipole surface charge method and the SPFD method in order to reduce the computational cost of dosimetry of electric field exposure. Specifically, in the developed method, the surface charge method in the first stage analyzes the surface charge induced on the surface of the human body, and the SPFD method in the second stage analyzes the induced electric field in the body caused by the surface charge. The fast multipole method is applied to the solution of the governing equations of the surface charge method, which is the most computationally expensive part of the method, to achieve high speed. As a result, it is shown that the developed method takes about 1/5 of the time and requires about 2/5 of the memory of the QS-FDTD method, which is a conventional method, and achieves the same level of computational accuracy.

Next, the consistency between the reference levels and the basic restrictions in the IEEE standard were verified by dosimetry using anatomical human body models of adult males and females. A spatially uniform magnetic field with the strength of the reference level was applied to the human body model in the frequency range of 0.5 Hz to 5 MHz, and the induced electric fields in the body were evaluated by dosimetry for the brain, heart, limbs, and other parts of the body that are subject to the basic restrictions of the standard. As a result, it was shown that in some parts of the body (heart, limbs, and other parts), the induced electric field strength in the body exceeded the basic restrictions. This result suggests that the reference levels of the IEEE standard for partial exposure to individual parts of the body do not have a margin of safety against the basic restrictions under whole-body exposure conditions.

Finally, the effect of the phase difference of electromagnetic fields on the induced electric field in the body under the condition of simultaneous exposure to electromagnetic fields was verified by dosimetry using anatomical human body models of adult man, woman, and child. Electric and magnetic fields with a frequency of 50 Hz, which are equivalent in strength to the reference level of ICNIRP guidelines and IEEE standards, were applied to the human body models, and the induced electric fields in the body were evaluated by dosimetry. The phase difference between the electric and magnetic fields was set between −90° and 90°. The analysis revealed that the induced electric field in the body varied according to the phase difference, and that the degree of variation depended on the region of the body. In addition, it is shown that the induced electric fields are below the basic restriction for the entire range of phase differences considered in this study under the simultaneous exposure conditions equivalent to the reference level of the ICNIRP guidelines. Based on these results, it is considered that even under conditions of simultaneous exposure to electromagnetic fields at the electric and magnetic field strengths (3 kV/m, 200 μT) specified in the Japanese ministerial ordinance as described in section 1.1.2, the induced electric field in the body is below the basic limit in the same guidelines because those are sufficiently lower than the reference level for public exposure in the ICNIRP guidelines (5 kV/m, 200 μT). On the other hand, the induced electric fields under the simultaneous exposure conditions at the reference level of the IEEE standard exceeded the basic restriction at some body parts, but this is because the reference level of the IEEE standard for magnetic fields does not have a margin to the basic restriction, as clarified in the verification described above.

The development of an efficient dosimetry method for electric fields in chapter 3 made it possible to evaluate the comprehensive impact of electromagnetic fields at low frequencies. Using this method, we were able to examine the issues related to the reference level of the international protection guidelines in chapter 4 and 5. The findings derived in this study will serve as a foothold for further elaboration of the international protection guidelines and will contribute to the safety of the general public around electric power facilities and workers involved in electric power operations.

In the future work, we plan to verify the effects of the superposition and phase difference of electromagnetic fields discussed in Chapter 5 under electromagnetic field exposure conditions assuming the actual posture of workers engaged in electric power maintenance work. In this case, the two-step computational method described in Chapter 3 using the fast multipole surface charge method and the SPFD method will be useful in the computation of induced electric fields in the body.

Acknowledgements

Firstly, I would like to express my sincere gratitude to my advisor Prof. Akimasa Hirata for the continuous support of my Ph.D. study and related research, for his patience, motivation, and immense knowledge. His guidance helped me in all the time of research and writing of this thesis.

Besides my advisor, I would like to thank the rest of my thesis committee: Prof. Shinji Yasui, Associate Professor Takashi Hikage at Hokkaido University for their insightful comments and encouragement, but also for the hard question which incented me to widen my research from various perspectives.

I would also like to express my deep gratitude to my secondary advisors, Prof. Yukio Mizuno and Associate Professor Sachiko Kodera, for their guidance and knowledge in environmental electromagnetic fields and dosimetry.

My sincere thanks also go to Prof. Essam Ali Hammam Ahmed Rashed, Dr. Yinliang Diao, Secretary Ritsuko Ishikawa and all of the laboratory member.

I would like to express my deep gratitude to Dr. Kenichi Yamazaki at the Central Research Institute of Electric Power Industry for leading me to this research area and for his constant guidance and encouragement. I am also deeply grateful to Dr. Takeo Shiina of the same institute for sharing his knowledge on dosimetry and computational electromagnetics, and for the valuable discussions we had.

I would like to thank everyone at my company Denryoku Computing Center, Ltd for approving and supporting my decision to pursue a doctoral degree while continuing to work.

Finally, I would like to thank my family for their understanding and constant emotional support for my doctoral studies.

References

[1] International Commission on Non-Ionizing Radiation Protection, “Exposure to static and low frequency electromagnetic fields, biological effects and health consequences (0 – 100 kHz),” ICNIRP 13/2003, Munich, 2003.

[2] International Commission on Non-Ionizing Radiation Protection, “Exposure to high frequency electromagnetic fields, biological effects and health consequences (100 kHz – 300 GHz),” ICNIRP 16/2009, Munich, 2009.

[3] M. Taki and S. Watanabe, “Review of guidelines on exposure limits of electromagnetic field exposure and exposure standards,” *J. Natl. Inst. Public Health*, vol. 56, no. 4, pp.363-370, 2007. (in Japanese)

[4] T. Shigematsu, “Trend of research on biological effects from ELF electromagnetic field exposure and exposure standards,” *IEEJ Journal*, vol. 128, no. 9, pp.623-626, 2008. (in Japanese)

[5] A. Hirata and O. Fujiwara, “Computational Tecniques of Electromagnetic Dosimetry for Humans,” *IEEJ Trans. FM*, vol. 129, no. 6, pp.391-395, 2009. (in Japanese)

[6] K. Yamazaki, M. Taki and C. Ohkubo, “Safety Assessment of Human Exposure to Intermediate Frequency Electromagnetic Fields,” *IEEJ Trans. FM*, vol. 135, no. 9, pp.500-506, 2015. (in Japanese)

[7] WHO, “Extremely Low Frequency Fields,” *Environmental Health Criteria*, no. 238, 2007.

[8] R. Matthes, E. van Rongen, and M. H. Repaholi, “Health Effects of Electromagnetic Fields in the Frequency Range 300 Hz to 10 MHz,” *ICNIRP*, Germany, 1999.

[9] International Commission on Non-Ionizing Radiation Protection, “Guidelines for limiting exposure to time-varying electric and magnetic fields (1 – 100kHz),” Health Phys., vol. 99, pp. 818-836, 2010.

[10] International Commission on Non-Ionizing Radiation Protection, “Guidelines for limiting exposure to time-varying electric and magnetic fields (100kHz – 300GHz),” Health Phys., vol. 118, pp. 483-524, 2020.

[11] IEEE Standard for Safety Levels with Respect to Human Exposure to Electric, Magnetic, and Electromagnetic Fields, 0 Hz to 300 GHz, IEEE Standard IEEE-C95.1TM-2019, 2019.

[12] Ministerial ordinance establishing technical standards for electric power equipment (電力設備に関する技術基準を定める省令（平成九年通商産業省令第五十二号）第二十七条・第二十七条の二) (in Japanese)

[13] J. Van Bladel, “Electromagnetic Fields Second Edition”, Wiley, 2007.

[14] J. P. Reilly, "Peripheral nerve stimulation by induced electric currents: Exposure to time-varying magnetic fields," *Med. Biol. Eng. Comput.* vol. 27, pp.101-110, 1989.

[15] Y. Suzuki, J. Gomez-Tames, Y. Diao and A. Hirata, "Evaluation of Peripheral Electrostimulation Thresholds in Human Model for Uniform Magnetic Field Exposure," *Int. J. Environ. Res. Public Health*, vol. 19, No. 1:390, Dec. 2021.

[16] K. Aga, A. Hirata, I. Laakso, H. Tarao, Y. Diao, T. Ito, Y. Sekiba, and K. Yamazaki, "Intercomparison of in situ Electric Fields in Human Models Exposed to Spatially Uniform Magnetic Fields," *IEEE Access*, vol. 6, pp. 70964-70973, 2018.

[17] T. W. Dawson and M. A. Stuchly, "High-resolution organ dosimetry for human exposure to low-frequency magnetic fields," *IEEE Trans. Magn*. vol. 34, no. 3, pp. 708-718, May 1998.

[18] P. J. Dimbylow, "Induced current densities from low frequency magnetic fields in a 2mm resolution, anatomically realistic model of the body," Phys. Med. Biol., vol. 43, pp. 221-230, 1998.

[19] R. Cech, N. Leitgeb, M. Pediaditis, "Fetal exposure to low frequency electric and magnetic field," Phys. Med. Biol., vol. 52, pp.879-888, 2007.

[20] A. Hirata, K. Wake, S. Watanabe, M. Taki, "In-situ electric field and current density in Japanese male and female models for uniform magnetic field exposures," Radiat. Prot. Dosimetry, vol. 135, no. 4, pp. 272-275, Aug. 2009.

[21] A. Hirata, Y. Takano, Y. Kamimura, and O. Fujiwara, "Effect of the averaging volume and algorithm on the in situ electric field for uniform electric- and magnetic-field exposures," Phys. Med. Biol., vol. 55, N243-N252, 2010.

[22] Y. Diao, J. Gomez-Tames, E. A. Rashed, R. Kavet, A. Hirata, "Spatial Averaging Schemes of In Situ Electric Field for Low-Frequency Magnetic Field Exposures." *IEEE Access*, vol. 7, pp. 184320-184331, 2019.

[23] J. Gomez-Tames, I. Laakso, Y. Haba, A. Hirata, D. Poljak, K. Yamazaki, "Computational Artifacts of the In Situ Electric Field in Anatomical Models Exposed to Low-Frequency Magnetic Field." *IEEE Trans. Electromagn. Compat*. vol. 60, no. 3, pp. 589-597, 2018.

[24] T. W. Dawson and M. A. Stuchly, "Organ dosimetry for human exposure to non-uniform 60-Hz magnetic fields," *IEEE Trans. Power Deliv.*, vol. 14, no. 4, pp. 1234–1239, Oct. 1999.

[25] O. P. Gandhi, G. Kang, D. Wu, and G. Lazzi, "Currents induced in anatomic models of the human for uniform and nonuniform power frequency magnetic fields," Bioelectromagn., vol. 22, pp. 112-122, Feb. 2001.

[26] T. W. Dawson, K. Caputa, and M. A. Stuchly, "Magnetic field exposures for UK live-line workers," *Phys. Med. Biol.*, vol. 47, no. 7, pp. 995–1012, Mar. 2002.

[27] M. A. Stuchly and T. W. Dawson, "Human body exposure to power lines: relation of induced quantities to external magnetic fields," Health Phys., vol. 83, no. 3, pp. 333–340, Sept. 2002.

[28] N. Maalej and C. Belhadj, "External and internal electromagnetic exposures of workers near high voltage power lines," Progress In Electromagnetics Research C, vol. 19, pp. 191-205, Feb. 2011.

[29] H. ElBidweihy and H. Anis, "Comparative exposure to magnetic fields of live-line workers on power lines," In Proceeding of the 2012 IEEE PES Transmission and Distribution Conference and Exposition (2012 PES T&D), Orlando, Florida, May 7-9, 2012.

[30] O. Bottauscio, A. Arduino, D. Bavastro, D. Capra, A. Guarneri, A. A. Parizia, and L. Zilberti, "Exposure of live-line workers to magnetic fields: A dosimetric analysis," Int. J. Environ. Res. Public Health, vol. 17, no. 7, Art. no. 2429, Apr. 2020.

[31] T. Shiina, T. Kudo, D. Herai, Y. Kuranari, Y. Sekiba, K. Yamazaki, "Calculation of Internal Electric Fields Induced by Power Frequency Magnetic Fields During Live-Line Working Using Human Models With Realistic Postures," IEEE Trans. Electromagn. Compat. vol. 63, no. 6, pp.1812-1819, Dec. 2021.

[32] C. M. Furse and O. P. Gandhi, "Calculation of electric fields and currents induced in millimeter-resolution human model at 60 Hz using the FDTD method," Biomagn., vol. 19, pp.293-299, 1998.

[33] T. W. Dawson, K. Caputa, M. A. Stuchly, "High-Resolution Organ Dosimetry for Human Exposure to Low-Frequency Electric Fields," *IEEE Trans. Pow. Del.*, vol. 13, no.2, pp.366-372, 1998.

[34] P. J. Dymbylow, "Current densities in a 2mm resolution anatomically realistic model of the body induced by low frequency electric fields," Phys. Med. Biol., vol.45, pp.1013-1022, 1999.

[35] A. Hirata, K. Caputa, T. W. Dawson, M. A. Stuchly, "Dosimetry in Models of Child and Adult for Low-Frequency Electric Field," IEEE Trans. Biomed. Eng., vol. 48, no.9, pp.1007-1012, Sept. 2001.

[36] A. Hirata and O. Fujiwara, "Dosimetry in Japanese male and female models for a low-frequency electric field," Phys. Med. Biol., vol. 52, pp.N339-N343, Aug. 2007.

[37] H. Tarao, L. H. Korpinen, H. A. Kuisti, N. Hayashi, J. A. Elovaara, and K. Isaka, "Numerical Evaluation of Currents Induced in a Worker by ELF Non-Uniform Electric Fields in High Voltage Substations and Comparison With Experimental Results," Bioelectromagn. 34:61-73, Jan. 2013.

[38] H. Tarao, H. Miyamoto, L. Korpinen, N. Hayashi, and K. Isaka, "Simple estimation of induced electric field in nervous system tissues for human exposure to non-uniform electric fields at power frequency," *Phys. Med. Biol.,* vol. 61, pp. 4438-4451, May. 2016.

[39] H. Tarao, A. Takei, N. Hayashi, and K. Isaka, "Electric Fields Induced inside Numerical Human Model Standing on Ground Plane with Elevated Arms in Uniform Electric Field at Power Frequency," *IEEJ Trans. FM*, vol. 138, no. 6, pp.322-328, 2018. (in Japanese)

[40] Y. Hamnerius, T. Nilsson, and E. Friman, "Evaluating exposure from electric fields in a high voltage switchyard according to the EU directive," *Journal of Radiological Protection*, vol.39, pp. 150-160, Jan. 2019.

[41] I. Laakso and T. Lehtinen, “Modeling and Measurement of Exposure to Realistic Non-Uniform Electric Fields at 50 Hz”, *2019 Joint International Symposium on Electromagnetic Compatibility, Sapporo and Asia-Pacific International Symposium on Electromagnetic Compatibility* (EMC Sapporo/APEMC), pp. 334-337, 2019.

[42] N. Leitgeb and R. Cech, “Dosimetric assessment of simultaneous exposure to ELF electric and magnetic fields,” *IEEE Trans. Biomed. Eng*., vol. 55, no. 2, pp. 671-674, Feb. 2008.

[43] R. Cech, N. Leitgeb, and M. Pediaditis, “Current densities in a pregnant woman model induced by simultaneous ELF electric and magnetic field exposure,” *Phys. Med. Biol.*, vol. 53, no. 1, pp.177-186, Jan. 2008.

[44] P. Kundur, “Power System Stability and Control (The EPRI Power System Engineering)”, McGraw-Hill, 1994.

[45] Committee for Standardization of Benchmark Power System Models, “Standard benchmark power system models,” IEEJ Technical Report, no. 754, 1999. (in japanese)

[46] T. Nagaoka, S. Watanabe, K. Sakurai, E. Kunieda, S. Watanabe, M. Taki, and Y. Yamanaka, “Development of realistic high-resolution whole-body voxel models of Japanese adult males and females of average height and weight, and application of models to radio-frequency electromagnetic dosimetry,” Phys. Med. Biol., vol. 49, pp. 1 – 15, Jan. 2004.

[47] T. Nagaoka, E. Kunieda, S. Watanabe, “Proportion-corrected scaled voxel models for Japanese children and their application to the numerical dosimetry of specific absorption rate for frequencies from 30 MHz to 3 GHz,” *Phys. Med. Biol*., vol. 53, pp. 6695 –6711, Dec. 2008.

[48] C. Gabriel, “Compilation of the dielectric properties of body tissues at RF and microwave frequency”, Technical Report of Brooks Air Force Base, AL/OE-TR-1996-0037, 1996.

[49] T. W. Dawson, J. De Moerloose, and M. A. Stuchly, “Comparison of magnetically induced ELF fields in humans computed by FDTD and scalar potential FD codes,” *Appl. Computational Electromagnetics Soc. J.*, vol. 11, no.3, pp. 63-71, 1996.

[50] H. A. Van der Vorst, “BI-CGSTAB: A fast and smoothly converging variant of BI-CG for the solution of nonsymmetric linear systems,” *SIAM J. Sci. Stat. Compt*., vol. 13, pp. 631 – 644, 1992.

[51] T. W. Dawson, M. Potter, and M. A. Stuchly, “Evaluation of modeling accuracy of power frequency field interactions with the human body,” *ACES Journal*, vol. 16, no. 2, pp. 162-172, 2001.

[52] Investigation Committee on Electric Field and Current Induced in a Human Body Exposed to Electromagnetic Fields, “Calculation of electric field and current induced inside a human body when exposed to an electromagnetic field,” IEEJ Technical Report, no. 1067, 2006. (in japanese)

[53] K. S. Yee, “Numerical solution of initial boundary value problems involving Maxwell's equations in isotropic media,” *IEEE Trans., Antennas & Propag*., vol.14, no.3, p.302-307, 1966.

[54] T. Uno, “Finite difference time domain method for electromagnetic field and antenna analyses, ” CORONA publishing, 1998. (in Japanese)

[55] J. Berenger, “A perfectly matched layer for the absorption of electromagnetic waves,” *Journal of Computational Physics,* vol.114, no.2, pp.185–200, 1994.

[56] S. D. Gedney, “An anisotropic perfectly matched layer-absorbing medium for the truncation of FDTD lattices,” *IEEE Trans. Antennas Propag*., vol. 44, no. 12, pp. 1630-1639, Dec. 1996.

[57] Italian National Research Council, “Calculation of the dielectric properties of body tissues in the frequency range 10 Hz - 100 GHz” [Online].Available:http://niremf.ifac.cnr.it/tissprop/htmlclie/htmlclie.php

[58] L. Greengard and V. Rokhlin, “A Fast Algorithm for Particle Simulations,” *J. Comp. Phys.*, vol. 73, pp.325-348, 1987.

[59] J. Makino and A. kawai, “REVIEW: Fast Multipole Method-Applications to Particle Systems,” *J. Appl. Mech*., vol. 2, pp.101-109, 1999.

[60] Y. Andoh, N. Yoshii, K. Fujimoto, K. Mizutani, H. Kojima, A. Yamada, S. Okazaki, K. Kawaguchi, H. Nagao, K. Iwahashi, F. Mizutani, K. Minami, S. Ichikawa, H. Komatsu, S. Ishizuki, Y. Takeda, and M. Fukushima, “MODYLAS: A Highly Parallelized General-Purpose Molecular Dynamics Simulation Program for Large-Scale Systems with Long-Range Forces Calculated by Fast Multipole Method (FMM) and Highly Scalable Fine-Grained New Parallel Processing Algorithms,” *J. Chem. Theory Comput*., vol. 9, pp.3201-3209, 2013.

[61] S. Hamada and T. Tadasu, “Application of Pseudo-particle Fast Multipole and Tree Methods to Surface Charge Method,” *IEEJ Trans. FM,* vol. 122, no.2, pp.178-185, 2002. (in Japanese)

[62] S. Hamada, “Fast-Multipole Surface-Charge-Simulation Method using Minor Iterative Preconditioning Technique,” *IEEJ Trans. FM*, vol. 124, no.2, pp.139-145, 2004. (in Japanese)

[63] S. Hamada and T. Kobayashi, “Analysis of Electric Field Induced by ELF Magnetic Field Utilizing Fast-Multipole Surface-Charge-Simulation Method for Voxel Data,” *IEEJ Trans. FM*, vol. 126, no.5, pp.355-362, 2006. (in Japanese)

[64] Y. Takahashi, “Large-scale electromagnetic field analysis by using integral equation method for practical electric machine design,” Waseda University Doctoral Degree Thesis, 2008.

[65] T. Tadasu and S. Hamada, “数値電界計算の基礎と応用” Tokyo Denki University Press, 2006. (in Japanese)

[66] T. W. Dawson, M. A. Stuchly, and R. Kavet, “Electric Fields in the Human Body Resulting From 60-Hz Contact Currents,” *IEEE Trans. Biomed. Eng*., vol. 48, no.9, pp.1020-1026, 2001.

[67] T. W. Dawson, K. Caputa, M. A. Stuchly, and R. Kavet, “Comparison of Electric Fields Induced in Humans and Rodents by 60-Hz Contact Currents,” *IEEE Trans. Biomed. Eng*., vol. 50, no.6, pp.744-752, 2002.

[68] J. De Moerloose, T. W. Dawson, and M. A. Stuchly, “Application of the finite difference time domain algorithm to quasi-static field analysis,” *Rad. Sci*., vol. 32, no. 2, pp.329-341, 1997.

[69] K. Yamazaki and Y. Sekiba, “Extension of calculation code for human exposure to electric and magnetic fields,” *IEEJ Technical Report* EMC13-076, 2013. (in Japanese)

[70] International Commission on Non-Ionizing Radiation Protection, "Guidelines for limiting exposure to time-varying electric and magnetic fields (up to 300GHz)," *Health Physics*, vol. 74, pp. 494-522, 1998.

[71] A. Rashed, Y. Diao, S. Tanaka, T. Sakai, J. Gomez-Tames and A. Hirata, "Effect of Skin-to-Skin Contact on Stimulation Threshold and Dosimetry," *IEEE Trans. Electromagn. Compat.*, vol. 62, no. 6, pp. 2704-2713, Dec. 2020.

[72] Y. Sekiba, K. Yamazaki, "Calculation Method of Electric Field Induced by ELF Electric Field in Human Bodies using Two-step Process Method Combining Fast-multipole Surface Charge and SPFD Methods," *IEEJ Trans. Fundam. Mater.*, vol. 139, no.7, p.309-318, Jul. 2019. (in Japanese)

[73] Y. Sekiba, K. Yamazaki, "Calculation of Internal Electric Fields Induced in Each Body Part of Human Models by ELF and Intermediate Frequency Uniform Magnetic Fields," *IEEJ Trans. Fundam. Mater.*, vol. 140, no.12, p.580-585, Dec. 2020.

[74] Y. Sekiba, S. Kodera, K. Yamazaki, and A. Hirata, "Calculation of Electric Field Induced in the Human Body for Simultaneous Exposure to Spatially Uniform ELF Electric and Magnetic Fields With a Phase Difference," *IEEE Access*, vol. 11, p. 95455-95466, 2023.

Publication Lists

Published Papers for Thesis

i. Y. Sekiba and K. Yamazaki, "Calculation Method of Electric Field Induced by ELF Electric Field in Human Bodies using Two-step Process Method Combining Fast-multipole Surface Charge and SPFD Methods," IEEJ Transactions on Fundamentals and Materials, vol. 139, no.7, pp.309–318, 2019. (in Japanese)

ii. Y. Sekiba and K. Yamazaki, "Calculation of Internal Electric Fields Induced in Each Body Part of Human Models by ELF and Intermediate Frequency Uniform Magnetic Fields," IEEJ Transactions on Fundamentals and Materials, vol. 140, no.12, pp.580–585, 2020.

iii. Y. Sekiba, S. Kodera, K. Yamazaki, and A. Hirata, "Calculation of Electric Field Induced in the Human Body for Simultaneous Exposure to Spatially Uniform ELF Electric and Magnetic Fields With a Phase Difference," IEEE Access, vol. 11, p. 95455-95466, 2023.

Peer Reviewed Journal Paper

iv. K. aga, A. Hirata, I. Laakso, H. Tarao, Y. Diao, T. Ito, Y. Sekiba, and K. Yamazaki, "Intercomparison of In Situ Electric Fields in Human Models Exposed to Spatially Uniform Magnetic Fields," IEEE Access Volume 6, Issue 1, pp.70964-70973, 2018.

v. T. Shiina, T. Kudo, D. Herai, Y. Kuranari, Y. Sekiba, K. Yamazaki, "Calculation of Internal Electric Fields Induced by Power Frequency Magnetic Fields During Live-Line Working Using Human Models With Realistic Postures," IEEE Transactions on Electromagnetic Compatibility, vol. 63, no. 6, pp. 1812-1819, Dec. 2021.

vi. Y. Diao, E. A. Rashed, L. Giaccone, I. Laakso, C. Li, R. Scorretti, Y. Sekiba, K. Yamazaki, and A. Hirata, "Intercomparison of the Averaged Induced Electric Field in Learning-Based

Human Head Models Exposed to Low-Frequency Magnetic Fields," IEEE Access Volume 11, pp. 38739-38752, 2023.

vii. A. Saito, T. Shiina and Y. Sekiba, "Estimation of Electric Field Inside a Neural Spheroid by Low-Frequency Magnetic Field Exposure," IEEJ Transactions on Electronics, Information and Systems, vol. 144, no.5, 2024. (to be published, in Japanese)

Peer Reviewed Conference Presentation for Thesis (Abstract)

viii. Y. Sekiba, K. Yamazaki, "Calculation of Internal Electric Fields Induced in Human Models by ELF and Intermediate Frequency Uniform Magnetic Fields," EMC Sapporo & APEMC 2019, TuePM1A.4, 2019. (Sapporo, Japan)

ix. Y. Sekiba, A. Hirata, K. Yamazaki, "Calculation of Internal Electric Field Induced by Simultaneous Exposure to Uniform ELF Electric and Magnetic Fields in Consideration of Phase Difference," URSI GASS 2023 SAPPORO, Commission K06, Aug. 2023. (Sapporo, Japan)

Peer Reviewed Conference Presentation (Abstract)

x. T. Shiina, Y. Sekiba, K. Yamazaki, "Evaluation of Internal Electric Fields in Human Head Exposed to Non-uniform Magnetic Fields in the Vicinity of Power Lines," URSI GASS 2023 SAPPORO, Commission K06, Aug. 2023. (Sapporo, Japan)

Appendix A: Effects of applying FMM on speedup

The speed-up effect of applying FMM on the time required to compute matrix-vector products when solving the surface charge method by the iterative method was verified compared to the case where FMM is not applied (i.e., direct computation). The computation time per matrix-vector product of the coefficient matrix and arbitrary vectors (T_{FMM} and $T_{non\text{-}FMM}$, respectively) of the surface charge method with and without FMM for a homogeneous conducting sphere under a uniform electric field of low frequency was compared by varying the number of surface elements N on the conducting sphere. As in the computations using the detailed human body model in Chapter 3, the leaf cells of the FMM are cubic regions made of 10 x 10 x 10 voxels, and the censoring order of the multipole expansion is 6.

Comparative results are shown in App. Fig. A.1 The figure also plots the speedup ratio (Speedup = $T_{non\text{-}FMM}$, / T_{FMM}). The results show that when N is less than about 10,000, the time required for computation without FMM is less than the time required with FMM (speedup ratio is less than a factor of 1), but when N is larger, the relationship is reversed and the speedup ratio is higher when FMM is applied. This may be because the hierarchical computation process of FMM becomes the rate-limiting cause when N is sufficiently small, and the total computation time is larger than when FMM is not applied. The speedup rate is approximately 60 times faster than that of the detailed human body model used in this study at about the same size (around N = 700,000).

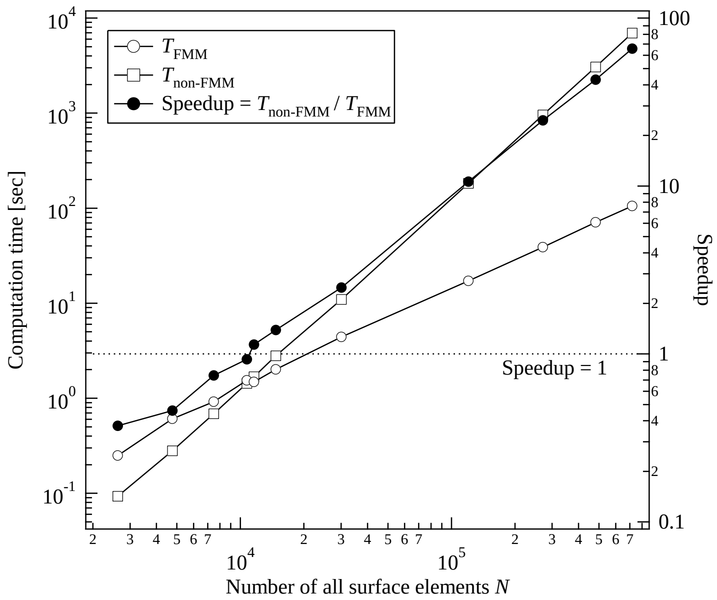

App. Figure A.1 Comparison of computation time for a matrix-vector product computation between those of FMM and non-FMM (without FMM) using homogeneous spherical conductor.

Appendix B:

Computational principle of the QS-FDTD method

The finite-difference time-domain (FDTD) method [53] is a numerical method for solving Maxwell's equations by direct differencing in time and space. When applying the FDTD method to an anatomical human body model with resolution ΔL [mm], the Courant condition [54] constrains the time step Δt to be $\Delta t \leq \Delta L / c$, where c is the speed of light. Thus, for ΔL = 2 [mm], Δt must be set to about $\Delta t = 10^{-12}$ [s]. At the frequency f = 50 [Hz], the number of steps required to compute one cycle is about $1/(f \cdot \Delta t) \sim 10^{10}$, which is extremely large and requires enormous computational resources.

The quasi-static FDTD method [68] uses a quasi-static approximation that neglects the displacement current, which significantly reduces the analysis time. The conservation law of electric charge is established at the surface of a human body placed in a low-frequency electric field as

$$\left(\sigma_{in}\boldsymbol{E}_{in} + \frac{\partial \boldsymbol{D}_{in}}{\partial t}\right)\cdot \boldsymbol{n} = \left(0 \cdot \boldsymbol{E}_{out} + \frac{\partial \boldsymbol{D}_{out}}{\partial t}\right)\cdot \boldsymbol{n} \tag{B.1}$$

where σ_{in} is the electrical conductivity of the human body, $\boldsymbol{E}_{in}$ and $\boldsymbol{E}_{out}$ are electric field in and out of the body, $\boldsymbol{D}_{in}$ and $\boldsymbol{D}_{out}$ are electric flux density in and out of the body, $\boldsymbol{n}$ is the normal vector of the body. Applying the condition of the quasi-static approximation that the displacement current term $\partial \boldsymbol{D}_{in}/\partial t = j\omega\varepsilon_{in}\boldsymbol{E}_{in}$ is sufficiently small and negligible compared to the conduction current term $\sigma_{in}\boldsymbol{E}_{in}$, we derive

$$\sigma_{in}\boldsymbol{E}_{in}\cdot \boldsymbol{n} = \frac{\partial \boldsymbol{D}_{out}}{\partial t}\cdot \boldsymbol{n} = j\omega\varepsilon_0 \boldsymbol{E}_{out}\cdot \boldsymbol{n} \tag{B.2}$$

This equation implies that the phase of the intduced electric field in the body $\boldsymbol{E}_{in}$ and external electric field $\boldsymbol{E}_{out}$ is shifted by $\pi/2$.

Here, since the wavelength of the electromagnetic field is sufficiently long compared to the size of the human body, the phase of the internal electric field is uniform throughout the body, and the phase of the external electric field is equal to the applied electric field and uniform throughout the outside. From this characteristic and Eq. (B.2), if the sinusoidal external electric field $\boldsymbol{E}_{out}(t) = \boldsymbol{E}_{out0} \exp(j\omega t)$ is replaced by a straight line with slope $\boldsymbol{E}_{out}'(t_0) = j\omega\boldsymbol{E}_{out0}$ at time t0 at its zero point, the internal electric field is constant at amplitude $\boldsymbol{E}_{in}(t_0)$. This $\boldsymbol{E}_{in}(t_0)$ is the induced electric field in the body to be derived.

Our quasi-static FDTD program [69] applies the FDTD method in the form of a scattering field [54] to achieve a uniformly varying electric field by providing the incident electric field with a linearly varying electric field. In addition, the Berenger's PML (Perfectly Matched Layer) absorbing boundary [54, 55] is used at the outermost region of the analysis space to reduce the effect of reflected waves.